Available online at www.CivileJournal.org

# Civil Engineering Journal

(E-ISSN: 2476-3055; ISSN: 2676-6957)

Vol. 12, No. 01, January, 2026

# Effect of Cu and $SiO_2$ on a Remelted-Recycled Piston Alloy Under Vertical Centrifugal Casting Conditions

Teguh Triyono [1], Eko Surojo [2*], Aditya Rio Prabowo [1, 2*], Triyono Triyono [1], Branislav Djordjevic [3], Hermes Carvalho [4, 5], Prayoga Wira Adie [1, 2], Muhammad Ilham Sholehuddin [1]

[1] *Department of Mechanical Engineering, Universitas Sebelas Maret, Surakarta 57126, Indonesia.*

[2] *Laboratory of Design and Computational Mechanics, Faculty of Engineering, Universitas Sebelas Maret, Surakarta 57126, Indonesia.*

[3] *Innovation Center of Faculty of Mechanical Engineering, Belgrade 11060, Serbia.*

[4] *Department of Structural Engineering, Federal University of Minas Gerais, Belo Horizonte 31270-901, Brazil.*

[5] *Department of Structural Engineering and Geotechnical, University of São Paulo, São Paulo 05508-020, Brazil.*

Received 07 May 2025; Revised 06 December 2025; Accepted 13 December 2025; Published 01 January 2026

**Abstract**

Functionally graded aluminum matrices produced by means of centrifugal casting offer a route to location-specific properties, yet sustainable feedstocks and dual-density reinforcements are less well explored. In this work, we evaluate vertical centrifugal casting (VCC) of a remelted, recycled piston alloy reinforced with silica ($SiO_2$) and copper (Cu) particulates selected for their contrasting densities relative to the matrix. Castings were produced at 1000 rpm for 5 minutes using a 500 °C preheated mold and an 800 °C pour temperature. Cu was added at 1–4 wt.% and $SiO_2$ was added at 0–9 wt.%. Bulk density/porosity measurements, Vickers hardness testing, and optical/SEM microstructural analysis were employed to characterize the resulting gradients. The density increased with the radial distance from the rotation axis, accompanied by a monotonic decrease in porosity, consistent with centrifugal separation. Microstructurally, $SiO_2$ concentrated toward the inner region near the rotation center; in comparison, Cu was enriched at the outer periphery. Correspondingly, hardness exhibited a spatial gradient: $SiO_2$-reinforced zones were hardest near the inner region, whereas Cu-rich outer zones were hardest at the external rim. These results demonstrate that VCC of a recycled Al–Si feedstock can be used to reliably tailor its microstructure and properties through density-driven particle segregation, enabling controllable, bidirectional functional grading using environmentally friendly starting materials.

*Keywords:* Vertical Centrifugal Casting; Remelting Piston; Cu Particle; Silica Sand; Functionally Graded Material (FGM).

## 1. Introduction

Vertical centrifugal casting (VCC) produces hollow, axisymmetric components through the rotation of a mold about a vertical axis with a stationary core defining the bore; the resulting centrifugal pressure head ($\Delta P \approx \rho\,\omega^2 r\,\Delta r$) assists metal delivery, enhances mold filling against gravity, and stabilizes the free surface, underpinning its widespread use in gears, impellers, pulleys, and wheels. Despite these advantages, VCC is susceptible to inner-radius defects: inadequate feeding may leave a weakly solidified central zone, and gas porosity is driven inward as bubbles experience an effective

* Corresponding author: esurojo@ft.uns.ac.id; aditya@ft.uns.ac.id

https://doi.org/10.28991/CEJ-2026-012-01-020

body force toward the rotation axis; in particle-reinforced castings, additional porosity can arise when limited wetting and capillary effects prevent molten Al from infiltrating inter-particle gaps at elevated local particle fractions [1–4]. The controllable parameters—superheat (pouring temperature), initial mold temperature, rotational speed ($\omega$), reinforcement loading and type, particle size/shape/aspect ratio, and alloy chemistry—govern process outcomes and together establish the thermal gradient ($G$) solidification front velocity ($R$), and mushy-zone permeability that dictate feeding, segregation, and defect evolution [5–7]. Increasing the pouring temperature reduces the melt viscosity ($\mu$), lowers the critical head for thin-section filling, and extends the window for particle migration before coherency; in turn, $\mu$ and $\omega$ couple with particle–matrix density contrast ($\Delta\rho$) through the centrifugal acceleration $a_c = r\omega^2$ to control Stokes-type drift, radial segregation, and the steepness of functional gradients in FGM castings [8].

Accordingly, quality can be improved via melt treatment and degassing to suppress inward gas transport, via mold/coating design and venting to stabilize flow, via optimization of $\omega$–temperature windows to balance filling and segregation, and via particle-surface conditioning to promote wetting and reduce interdendritic porosity—measures that enable VCC to deliver hollow components with deliberately tailored property gradients while mitigating characteristic inner-region defects. Compared with conventional monolithic alloys and particulate/laminate composites that deliver essentially uniform properties, continuous or stepwise spatial variations in composition and microstructure are deliberately engineered in functionally graded materials (FGMs) to place stiffness, strength, wear resistance, or thermal conductivity exactly where they are most needed [9–11]. In joining or transition zones between dissimilar and otherwise incompatible materials (e.g., ceramic–metal or Cu–Al systems), FGMs mitigate sharp modulus and thermal-expansion mismatches, thereby reducing interfacial residual stresses and improving bonding and durability relative to discrete coatings or adhesive layers [10, 12].

Among fabrication routes (such as powder metallurgy with controlled layering, spark plasma sintering, infiltration, thermal spraying, and graded-feed additive manufacturing) centrifugal casting is frequently preferred for axisymmetric parts because it leverages density-driven segregation to form robust radial gradients in a single melt step, offering high throughput, low material waste, and favourable economics [13–17]. While powder-based and additive manufacturing (AM) routes provide fine spatial control and non-axisymmetric gradients, they often entail higher equipment cost, slower build rates, and post-processing to achieve full density and metallurgical quality; by contrast, vertical or horizontal centrifugal casting readily attains near-full density and metallurgical bonding but is primarily limited to ring- or tube-like geometries and requires careful control of pouring temperature, mold preheat, rotational speed, and reinforcement attributes to manage porosity and gradient sharpness [18–20]. Consequently, the centrifugal route complements rather than replaces alternative FGM processes. It is exceptionally competitive, with a focus on radial property grading, scalability, and cost-effectiveness. In contrast, powder- and AM-based methods remain advantageous for complex gradient architectures, sharp multi-material interfaces, or intricate shapes that depart from rotational symmetry. Nevertheless, based on recent works summarized in [21-26], functionally graded materials are being processed and manufactured from new materials, with titanium the dominant material (see Table 1). The literature remains fragmented, and there is growing demand for greater comprehension of the effects of recycled and remelted objects on the outcomes of vertical centrifugal casting.

**Table 1. Summary of research milestones in vertical centrifugal casting**

| References | Keywords | Material | Notable results |
|---|---|---|---|
| Mazloum et al. [21] | • Vertical centrifugal casting<br>• A356 alloy<br>• A413 alloy<br>• Thermo-fluid | A413 and A356 alloys | Porosity decreases with an increase in the aspect ratio up to 2, accompanied by the lowest interface heat transfer coefficients observed at 6867.62 W/(m2·K) for A413 and 7703.89 W/(m2·K) for A356. |
| Shen et al. [22] | • Vertical centrifugal casting<br>• Fluid frontal motion morphology | Titanium alloy | With an increase in centrifugal speed, simultaneously and at the same position, the flow width of the simulated fluid in the runner is gradually narrowed, the cross-sectional area of the fluid steadily reduces, and the blank flow area of the fluid inside the runner slowly increases. |
| Ling et al. [23] | • Vertical centrifugal casting<br>• Shrinkage prediction<br>• Pressure distribution | Ti-6Al–4V alloy | The shrinkage cavities tend to accumulate near the rotation axis because the zero isostatic surface tends to approach the rotation axis as the rotation speed increases. |
| Liao et al. [24] | • Vacuum centrifugal casting<br>• Ring rolling<br>• δ phase | IN718 superalloy | Under high-vacuum and high-centrifugal-field conditions, the as-cast IN718 ring blanks exhibited fine (ASTM 4) and uniformly distributed equiaxed grains without macroscopic defects. |
| Changyun et al. [25] | • Vertical centrifugal casting<br>• Filling length<br>• Rotational velocity<br>• Inner defects | Titanium Alloy | Different rotational directions result in distinct filling sequences of molten metal, which in turn affect the subsequent solidification and the formation of defects. |
| Changyun et al. [26] | • Vertical centrifugal casting<br>• Alloy melts<br>• Cavity wall<br>• Liquid crash<br>• Coriolis force | Titanium alloy | With the action of centrifugal force and Coriolis force, the liquid adheres to one side of the runner or cavity wall, filling it. The wall is opposite to the rotational direction. |

Addressing sustainability and circular-materials goals, in this study, we investigate vertical centrifugal casting (VCC) of a remelted end-of-life Al–Si automotive piston alloy as a low-impact feedstock for functionally graded components. To exploit density-driven segregation during VCC and thereby tailor radial property gradients, we performed a parametric addition of copper (Cu; 0, 1, 2, 3, and 4 wt.%)—denser than the matrix—and silica sand ($SiO_2$; 0, 3, 6, and 9 wt.%)—less dense than the matrix. The resulting castings were sectioned from the outer to the inner radius into four concentric segments and subjected to macro- and micro-scale characterization to quantify physical and mechanical gradients, including density/porosity measurements, hardness testing, and microstructural examinations to elucidate how reinforcement type and loading interact with centrifugal processing to control particle distribution, defect formation, and property evolution across the wall thickness. The structure of the current research is divided into five primary sections, namely, the Introduction, which consists of the background and summarized pioneer works; Research Methodology, in which the details of the research materials, processes, specimens, and stages are explained; Testing Results and Discussion, in which the mechanical behaviors of the specimens are discussed according to the input parameters; Microstructural Observation and Analysis, in which we present the microstructure photographs after the specimens were tested; and the Conclusions, in which all findings are summarized based on the obtained phenomena.

## 2. Research Methodology

The research workflow commenced with a comprehensive literature study and review to identify the scientific background, relevant parameters, and existing gaps in the field of centrifugal casting of recycled aluminum alloys. Based on this review, the appropriate specimen materials were selected and prepared, including the recycled piston alloy as the matrix and the added copper and silica particles with various weight fractions. The prepared materials were then processed through the casting stage using the designed centrifugal casting setup to produce functionally graded specimens. After casting, a series of tests was conducted to evaluate the density and porosity behaviors, in addition to the hardness characteristics, across different specimen segments. These results were followed by detailed observations, focusing on microstructural features and the specific effects of copper and silica additions on particle distribution and defect formation. Lastly, the combined testing and observational data were interpreted to determine the resulting mechanical properties and phase morphology. The described processes are summarized in Figure 1.

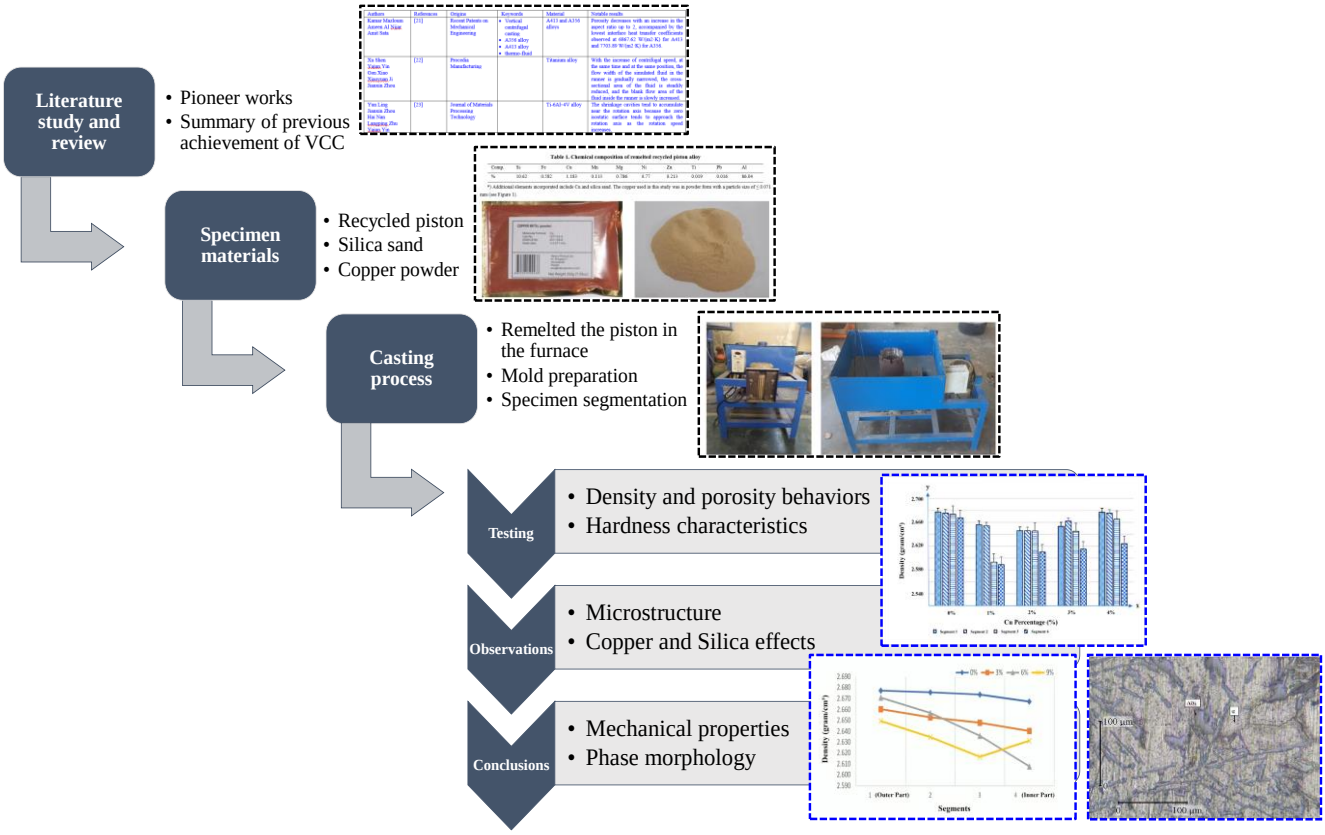


**Figure 1. Flowchart of the current methodological research**

### 2.1. Deployed Materials

The base material used in this study was derived from remelted–recycled piston alloy cast into ingots. A spectrometer analysis was then conducted to determine its composition, as presented in Table 2.

**Table 2. Chemical composition of the remelted–recycled piston alloy**

| Comp. | Si | Fe | Cu | Mn | Mg | Ni | Zn | Ti | Pb | Al |
|---|---|---|---|---|---|---|---|---|---|---|
| % | 10.62 | 0.582 | 1.183 | 0.113 | 0.786 | 0.77 | 0.213 | 0.019 | 0.016 | 86.04 |

Additional elements incorporated include Cu and silica sand. The copper used in this study was in powder form with a particle size of ≤ 0.071 mm (see Figure 2).


(a) (b)

**Figure 2. Added materials: (a) Copper powder and (b) silica sand particles (Argyia Murni filter, Jakarta, Indonesia)**

The silica sand powder used as a reinforcement in the Al-Si alloy was sieved to achieve a particle size of 200 mesh (≤0.074 mm). The composition of the silica sand is presented in Table 3.

**Table 3. Silica sand composition**

| SQX Calculation Results | | | |
|---|---|---|---|
| **Sample** | SP24079208011 | **Data Analyzed** | 2024-5-14 10:08 |
| **Application** | Powder | **Sample Type** | Oxide Powder |
| **Balance** | Estimate | | |
| **Matching Library** | | **Impurity Corr.** | |
| **Density** | 1333.9165 mg/cm$^2$ | **Diameter** | 30.0 mm |
| **Helium Corr.** | Yes | | |
| **Weight** | 9.4289 g | | |

| Sample Film Corr. | P. P. Film |
|---|---|
| File | SP24079208011 |
| Height | 10.0 mm |

| No. | Component | Result | Unit | El. line | Intensity | Analyzing Depth |
|---|---|---|---|---|---|---|
| 1. | Total | 13.30 | mg/cm$^2$ | - | - | - |
| 2. | $AL_2O_3$ | 2.40 | Mass % | Al-KA | 1.5244 | 0.0101 |
| 3. | $SiO_2$ | 67.6 | Mass % | Si-KA | 43.0445 | 0.0139 |
| 4. | $SO_3$ | 0.0443 | Mass % | S-KA | 0.0459 | 0.0151 |
| 5. | Cl | 0.0118 | Mass % | Cl-KA | 0.0480 | 0.0199 |
| 6. | $K_2O$ | 0.211 | Mass % | K-KA | 0.3521 | 0.0453 |
| 7. | CaO | 0.151 | Mass % | Ca-KA | 0.3994 | 0.0604 |
| 8. | $TiO_2$ | 0.108 | Mass % | Ti-KA | 0.0693 | 0.1012 |
| 9. | $Fe_2O_3$ | 0.216 | Mass % | Fe-KA | 1.0291 | 0.2739 |
| 10. | NiO | 0.0096 | Mass % | Ni-KA | 0.0989 | 0.4270 |
| 11. | Balance | 29.3 | Mass % | Pd-KAC | 10.6277 | - |

## 2.2. Casting Equipment and Process

In this study, the casting process was conducted using the centrifugal casting method, with a mold rotation speed of 1000 rpm, a pouring temperature of 800 °C, and a preheating temperature of 450 °C. The casting process is described step by step as follows:

- Aluminum is melted in a resistance furnace to a temperature of 800 °C combined with the aluminum melting process; the mold is installed on the centrifugal casting machine and heated.
- When the aluminum temperature has reached 800 °C, additional elements (Cu or $SiO_2$) are added and then stirred with a blade for 1 minute.
- The molten metal is poured into the mold at a pouring temperature of 800 °C that has been installed on the centrifugal machine when the mold preheat temperature has reached 450 °C.
- The mold is closed, and the centrifugal machine is turned on at 1000 rpm.
- After being rotated for 5 minutes, the centrifugal casting machine is turned off and time is provided for the mold to reach room temperature. Thereafter, the cast metal is removed from the mold. The machine deployed for casting is presented in Figure 3.

**Figure 3.Vertical centrifugal casting machine**

Thereafter, the process of specimen treatment/refinement for further testing is described as follows:

- The cast specimen was cut cross-sectionally, as shown in Figure 4. Each cast object was cut into four segments with dimensions of 3 cm × 1 cm × 1 cm (P × W × H).
- In each segment, three tests were performed (density, hardness, and microstructure tests).
- Density testing was performed with reference to Archimedes' law. The tools used for density testing were vibrating scales of type AJ-620E and a breaker glass filled with water.
- In the Brinell hardness test, the ASTM E-10 standard was applied. The indenter diameter was 2.5 mm, and the load was 62.5 kg, with a loading time of 30 seconds


**Figure 4. Results of the casting process and designation of specimen number**

- Microstructure observations were performed based on the ASTM E407 standard using a Keller reagent etching solution: 2 mL of HF + 3 mL of HCl + 5 mL of $HNO_3$ + 190 mL of distilled water. The test procedure was as follows:
  - The surface of the test specimen was smoothed with sandpaper.
  - The surface of the test specimen was polished with Autosol and a cloth.
  - The specimen was dipped into Keller's reagent etching solution for 10–15 seconds and then washed with flowing water.
  - Specimens in Segments 1 to 4 (as shown in Figure 5) were observed using an optical microscope to take micro-photos

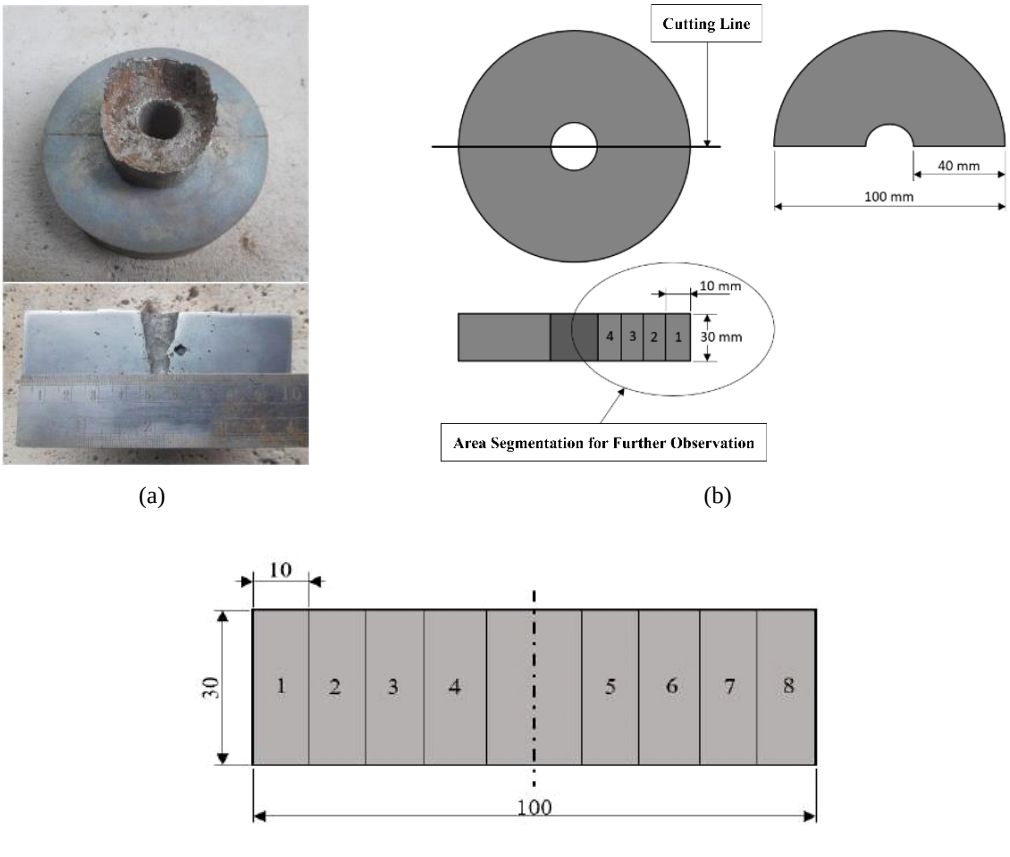


**Figure 5. Specimen details for testing: (a) Result of the centrifugal casting process, (b) specimen cutting method for testing, and (c) segmentation of specimen number for further testing**

## 2.3. Testing Standards and Specimen Images

The Brinell hardness test was conducted using a 2.5 mm diameter solid ball indenter with a 62.5 kgf load, in accordance with the ASTM E10 standard [27]. Hardness measurements were taken at three points on each specimen segment, and the average value was calculated. Microstructural analysis was performed based on the ASTM E407 standard using Keller's etchant solution, which comprises 2 mL of HF, 3 mL of HCl, 5 mL of $HNO_3$ , and 190 mL of distilled water [28].

## 2.4. Testing Standards and Specimen Images

In this study, Cu particles were added with varying weight fractions of 0 wt.%, 1 wt.%, 2 wt.%, 3 wt.%, and 4 wt.%. Moreover, silica sand was incorporated with weight fractions of 0 wt.%, 3 wt.%, 6 wt.%, and 9 wt.%. To analyze the gradient of mechanical and physical properties, testing was conducted on four segments, from the outer to the inner region. The segmentation for testing is illustrated in Figure 4. The centrifugal castings with various additions of Cu particles and silica sand were analyzed using three types of tests: density measurement, microstructural analysis, and hardness testing.

### 2.5. Theoretical Approach: Addition of Copper

The effect of adding copper to aluminum alloys can mainly be explained by solid-solution strengthening and precipitation-hardening mechanisms. When Cu is added, Cu atoms initially dissolve into the Al matrix, creating lattice distortions due to the difference in atomic size and electronic structure between Al and Cu; these distortions hinder dislocation motion and increase strength (solid-solution strengthening) [29, 30]. Upon suitable heat treatment (solutionizing and ageing), the supersaturated Al–Cu solid solution decomposes to form Guinier–Preston (GP) zones and then metastable θ″ and θ′ precipitates before finally transforming into the stable $Al_2Cu$ (θ) phase, as widely reported in studies of Al–Cu and 2xxx series alloys [31, 32]. The fine, coherent, and semi-coherent precipitates act as substantial obstacles to dislocation motion, thereby significantly increasing yield strength and hardness. However, if the Cu content is too high or ageing is not well controlled, coarse $Al_2Cu$ particles and continuous grain-boundary networks may form, promoting intergranular fracture, reducing ductility, and increasing susceptibility to localized corrosion [33, 34]. Thus, from a theoretical standpoint, copper addition strengthens aluminum primarily through precipitation hardening; however, its content and heat-treatment parameters must be carefully optimized to avoid excessive brittleness and corrosion issues.

### 2.6. Theoretical Approach: Addition of Silica Sand

The addition of silica sand ($SiO_2$) particles to aluminum alloys modifies the material's behavior through metal–matrix–composite strengthening mechanisms. As a stiff, challenging ceramic phase, $SiO_2$ does not plastically deform like the Al matrix; instead, it carries part of the applied load and constrains matrix deformation, thereby producing an effective load-transfer mechanism that increases stiffness and hardness [35, 36]. The substantial mismatch in elastic modulus and thermal expansion between $SiO_2$ and aluminum generates high dislocation densities around the particles during solidification and cooling, which further strengthens the alloy via geometrically necessary dislocations and dislocation pile-up at the particle–matrix interface [37, 38]. In cast systems, well-dispersed silica particles can also serve as heterogeneous nucleation sites, promoting grain refinement and improving strength and dimensional stability at elevated temperatures [39]. However, because $SiO_2$ is brittle and relatively inert, excessive particle content or poor interfacial bonding may lead to agglomeration, interfacial debonding, and microcrack initiation, ultimately reducing ductility and fracture toughness. In centrifugal-cast or functionally graded configurations, the lower density of $SiO_2$ relative to aluminum drives segregation toward the inner region of the casting, producing a gradient where the inner zone becomes harder and more wear-resistant but potentially more brittle than the outer, matrix-rich region, consistent with general FGM theory for particle-reinforced aluminum systems [40].

## 3. Testing Results and Discussions: Density and Porosity

### 3.1. Effect of Copper (Cu) Addition

The density test results of Al-Si alloy castings with copper addition are presented in Figures 6a and 6b. The obtained densities for specimens with 0 wt.%, 1 wt.%, 2 wt.%, 3 wt.%, and 4 wt.% copper addition generally decreased from Segment 1 (outer diameter) to Segment 4 (inner diameter). The highest density was observed in the specimen with 0 wt.% copper addition in Segment 1, with a density of 2.677 g/cm³. In comparison, the lowest density was observed in the specimen with 1% copper addition in Segment 4, at 2.589 g/cm³. Two main phenomena can be identified from these results: (i) a general decrease in density with increasing Cu content and (ii) a density difference between the outer and inner regions, where the outer region consistently exhibits higher density. The first phenomenon, the reduction in density with higher Cu content, can be explained using casting and solidification theory, particularly in terms of the role of gas porosity and melt fluidity. Copper addition tends to increase hydrogen solubility and hydrogen gas pressure in the melt, promoting the formation of gas porosity during solidification, as widely noted for Al–Cu and Al-Si-based casting alloys [41-43]. As solidification progresses, interdendritic feeding becomes more difficult in a less fluid melt; therefore, any entrapped gas or shrinkage cavities are not fully compensated by liquid metal flow. This accumulation of gas pores and microvoids reduces the effective mass per unit volume, thereby lowering the measured density, consistent with general descriptions of porosity formation and feeding limitations in aluminum castings [44, 45]. This adverse effect of Cu addition on porosity and density is evident in Figures 6c and 6d, whereby higher Cu contents are associated with higher porosity levels. In casting theory, such behavior is consistent with the formation of gas and shrinkage porosity in alloys with reduced fluidity and hindered feeding, in particular when the cooling rate and solidification time do not allow sufficient escape of dissolved gases [46].

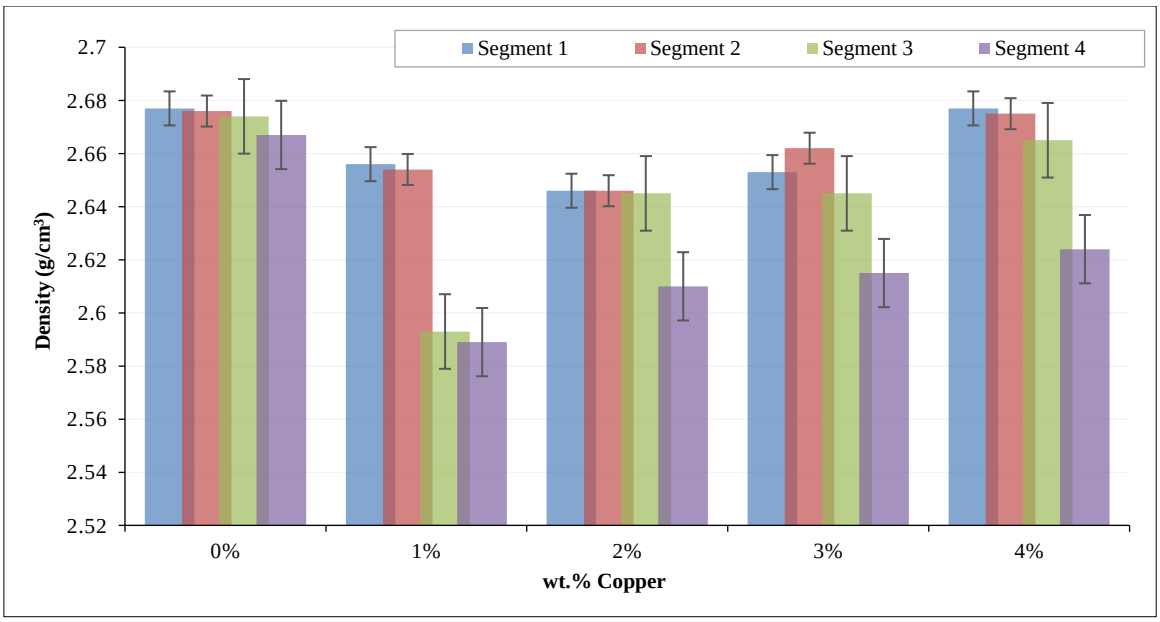
Segment 1
Segment 2
Segment 3
Segment 4
Density (g/cm³)
2.7
2.68
2.66
2.64
2.62
2.6
2.58
2.56
2.54
2.52
0%
1%
2%
3%
4%
wt.% Copper

(a)

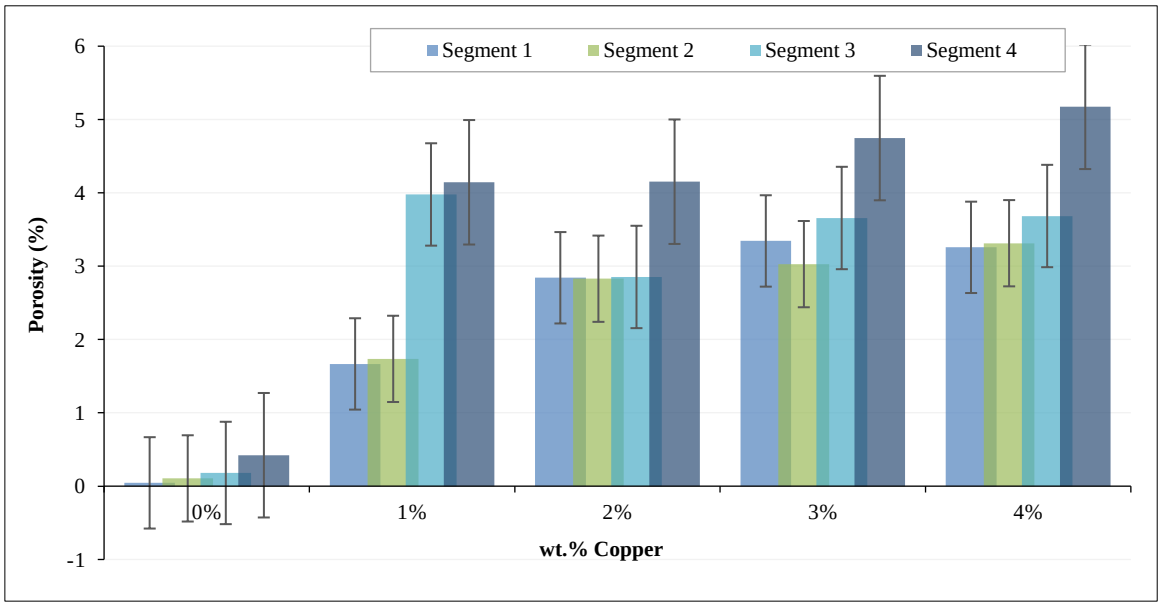
Segment 1
Segment 2
Segment 3
Segment 4
Porosity (%)
6
5
4
3
2
1
0
-1
0%
1%
2%
3%
4%
wt.% Copper

(b)

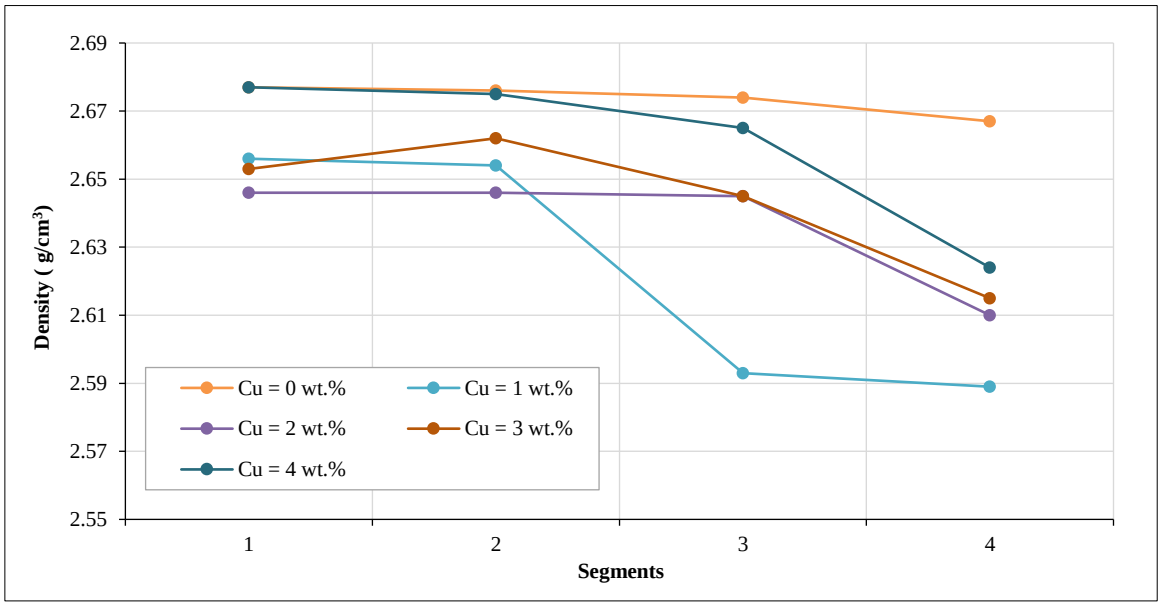
Density ( g/cm³)
2.69
2.67
2.65
2.63
2.61
2.59
2.57
2.55
1
2
3
4
Segments
Cu = 0 wt.%
Cu = 1 wt.%
Cu = 2 wt.%
Cu = 3 wt.%
Cu = 4 wt.%

(c)

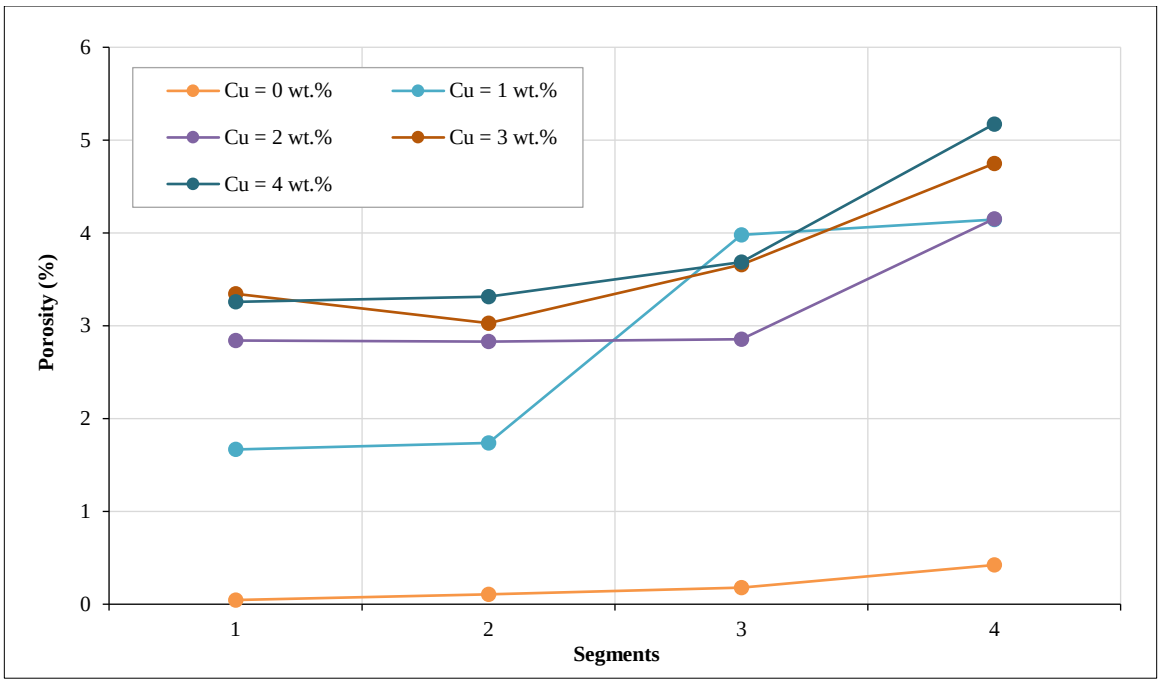


(d)

**Figure 6. (a) Density graph as a function of Cu addition, (b) density variation due to Cu addition, (c) density distribution across segments with Cu addition, and (d) porosity trend across segments with Cu addition**

The second phenomenon, whereby the outer region exhibits a higher density than the inner region, can be directly correlated with the principles of centrifugal casting and centrifugal segregation. Under rotational motion, the molten metal and any solidifying particles are subjected to a radial acceleration directed outward from the axis of rotation. In this condition, particles or phases with higher density—such as Cu-rich regions or intermetallics in the Al-Si-Cu system—experience a greater centrifugal force and tend to migrate toward the outer circumference of the mold. This segregation mechanism leads to a higher concentration of dense constituents and a more compact microstructure in the outer segment (Segment 1), resulting in a higher measured density, which is consistent with reports on functionally graded Al-based composites produced by means of centrifugal casting [47]. Conversely, the inner segment (Segment 4) becomes relatively depleted of these heavier particles. It may also retain more porosity due to lower adequate pressure and weaker feeding, which further reduces its density. This radial density gradient from outer to inner regions is a typical characteristic of vertical centrifugal casting, where both density differences between phases and centrifugal acceleration govern particle distribution during solidification [48]. Therefore, the experimental trends shown in Figures 6a–6d are in close agreement with fundamental casting theory, which states that the addition of copper increases porosity. It reduces density through its influence on gas evolution and fluidity, whereas centrifugal force drives denser phases outward, resulting in a functionally graded density profile across the casting radius.

### 3.2. Effect of Silica ($SiO_2$ ) Addition

The density test results based on $SiO_2$ addition are presented in Figures 7a and 7b; in comparison, in Figures 7c and 7d, the corresponding porosity calculations are shown (variation numbers 1 to 4 equal to 0, 3, 6, and 9 wt.% $SiO_2$ addition, consecutively). The effect of silica sand particle addition was evaluated along the specimen's cross-section from Segment 1 (outer region) to Segment 4 (inner region). For the base alloy without $SiO_2$ (0 wt.%), the density is 2.677 g/cm³ at the outer region and decreases slightly to 2.667 g/cm³ at the inner region. With 3 wt.% $SiO_2$, the density becomes 2.660 g/cm³ (outside) and 2.640 g/cm³ (inside). At 6 wt.% $SiO_2$, the densities are 2.671 g/cm³ (outside) and 2.608 g/cm³ (inside), showing a more pronounced decrease toward the inner segment. For 9 wt.% $SiO_2$, the density is 2.649 g/cm³ on the outside and 2.631 g/cm³ on the inside. Overall, despite some local fluctuation, the general tendency shown is that the outer region remains denser than the inner region, and the inner density becomes more sensitive to $SiO_2$ content. This density trend with $SiO_2$ addition is consistent with the previously observed behavior for Cu, whereby density tends to decrease toward the inner region in parallel with an increase in porosity.

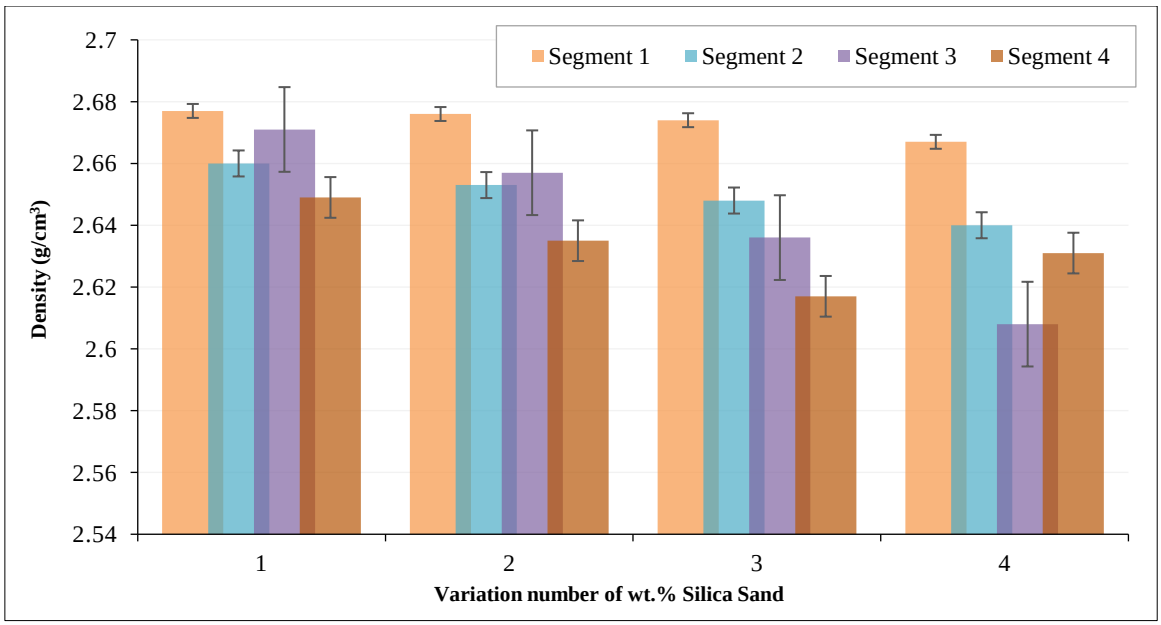
Segment 1
Segment 2
Segment 3
Segment 4
Density (g/cm³)
2.7
2.68
2.66
2.64
2.62
2.6
2.58
2.56
2.54
1
2
3
4
Variation number of wt.% Silica Sand

(a)

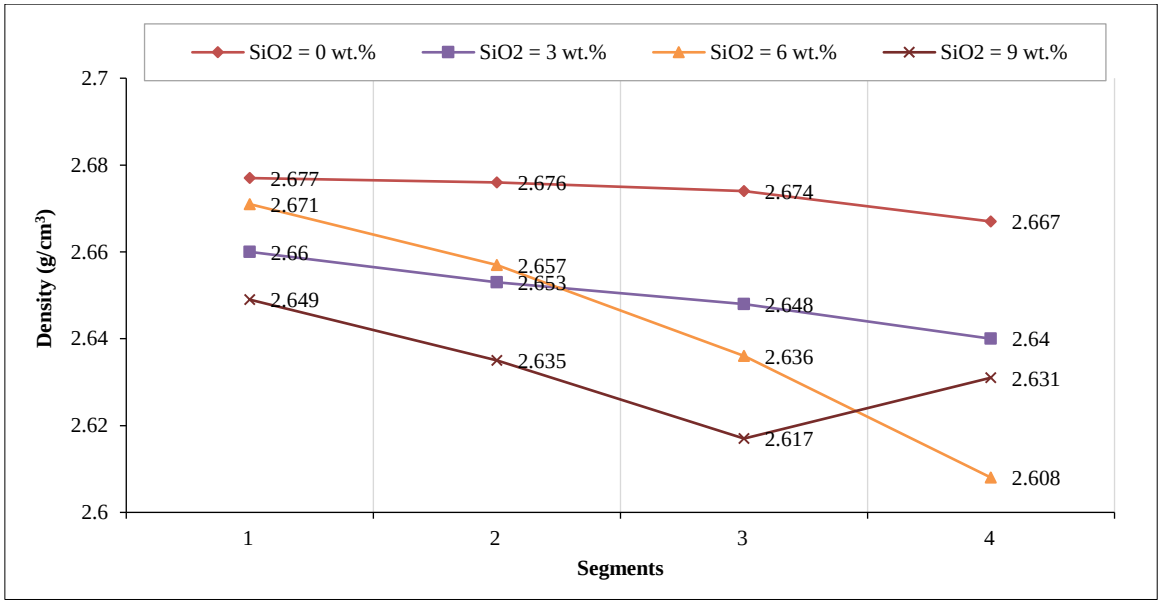
SiO2 = 0 wt.%
SiO2 = 3 wt.%
SiO2 = 6 wt.%
SiO2 = 9 wt.%
Density (g/cm³)
2.7
2.68
2.66
2.64
2.62
2.6
2.677
2.676
2.674
2.667
2.671
2.657
2.636
2.608
2.66
2.653
2.648
2.64
2.649
2.635
2.617
2.631
1
2
3
4
Segments

(b)

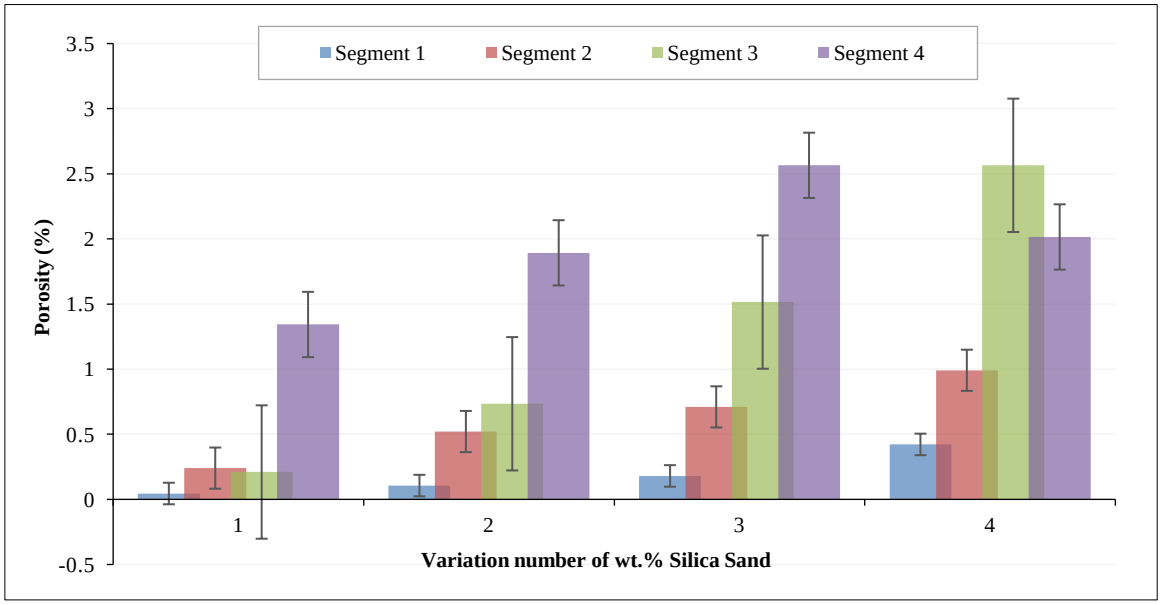
Segment 1
Segment 2
Segment 3
Segment 4
Porosity (%)
3.5
3
2.5
2
1.5
1
0.5
0
-0.5
1
2
3
4
Variation number of wt.% Silica Sand

(c)

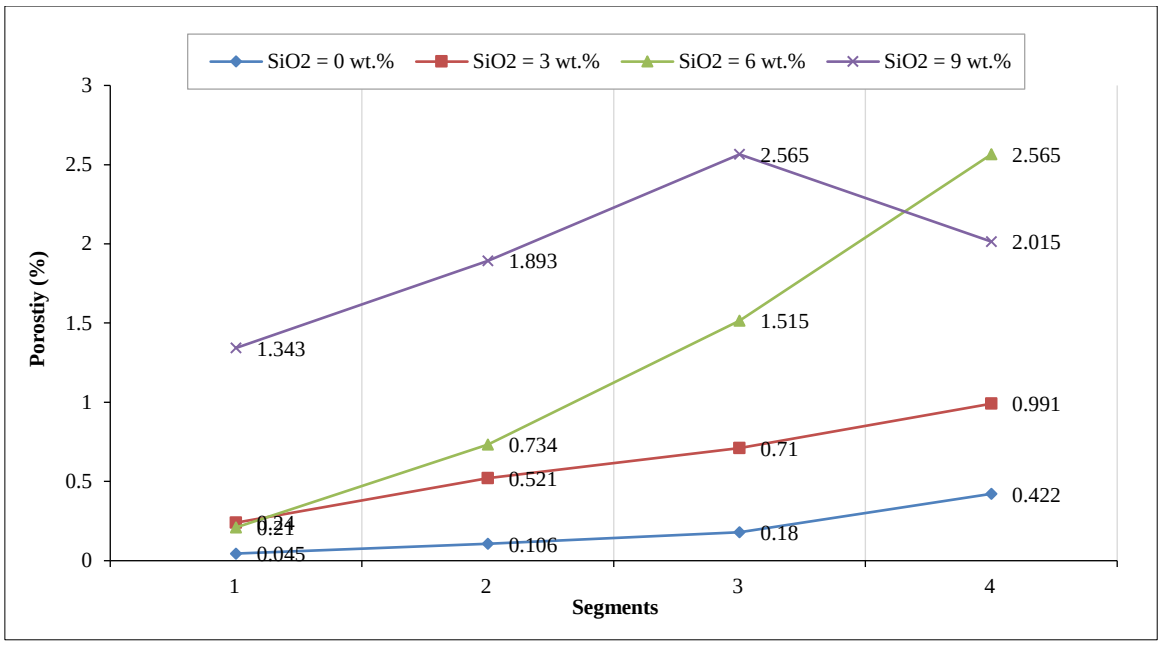


(d)

**Figure 7. (a) Density graph as a function of silica sand addition, (b) density distribution across segments with $SiO_2$ addition, (c) porosity variation due to silica sand addition, and (d) porosity trend across segments with $SiO_2$ addition**

From a theoretical standpoint, this behavior can be interpreted using composite theory and centrifugal casting principles. In terms of material properties, the density of $SiO_2$ particles (≈ 2.65 g/cm³) is slightly lower than that of the Al–Si matrix (≈ 2.7 g/cm³) [6, 49-54]. Based on the rule of mixtures for particulate-reinforced metal matrix composites, introducing a phase with lower density will reduce the overall composite density when the particle volume fraction increases. Moreover, in a centrifugal casting process, phases with different densities experience different radial accelerations. Heavier constituents (the liquid Al–Si matrix) are more strongly driven outward, whereas lighter $SiO_2$ particles tend to remain closer to the inner region or are less efficiently transported outward, resulting in a relative enrichment of $SiO_2$ in the inner segments and a corresponding decrease in density, especially at higher particle contents. Concurrently, the outer region remains matrix-rich, more compact, and therefore slightly denser.

The porosity results presented in Figures 7c and 7d further support this explanation and are consistent with solidification and feeding theories for particle-reinforced castings. $SiO_2$ particles, being ceramic and relatively poorly wetted by molten aluminum, can act as obstacles to interdendritic feeding and as potential nucleation sites for microvoids. As solidification progresses, the presence of rigid, non-deformable particles increases flow resistance and can locally trap liquid films and gases, thereby promoting porosity formation when feeding is insufficient. In regions where the $SiO_2$ concentration is higher (typically closer to the inner region due to lower density and centrifugal segregation), this effect becomes more pronounced, resulting in higher porosity and, consequently, a lower measured density. The approximate relationship $\rho_{measured} \approx \rho_{dense} \cdot (1 - P)$, where P is porosity, explains why regions with higher porosity (inner segments at higher $SiO_2$ contents) exhibit lower density values.

From the above results, it can be concluded that the experimental trends presented in Figures 7a–7d are consistent with related theories of (i) density evolution in particle-reinforced metal matrix composites (rule of mixtures), (ii) centrifugal segregation driven by density differences between the matrix and reinforcement, and (iii) porosity formation in castings with hindered feeding due to solid particles and limited melt fluidity. The addition of $SiO_2$, with slightly lower density than the matrix and limited wettability, not only decreases the composite density through its intrinsic density but also indirectly reduces density by increasing porosity, particularly in the inner region where particle accumulation and reduced feeding are more likely to occur. The density difference between constituent materials influences the final composite density, resulting in a density gradient across the specimen's cross-section. The centrifugal force affects the density distribution, thereby causing variations in the final density along the specimen [55, 56]. Gas porosity occurs as the centrifugal force pushes gas toward the inner region of the specimen [57-63]. Pores in the composite form due to gaps between reinforcing particles that remain unfilled by molten aluminum, a primary cause of porosity in the composite [64]. Matrix porosity arises from both gas porosity and shrinkage porosity.

Gas porosity results from reactions between the molten metal and the mold, in addition to gas entrapment during the solidification process. Shrinkage porosity, in contrast, is related to the liquid-to-solid volume fraction and the alloy's solidification temperature range [65]. Centrifugal force further exacerbates gas porosity, which drives trapped gases toward the inner region of the specimen [66-69].

## 4. Testing Results and Discussion: Hardness Characteristic

The hardness test results, as shown in Figure 8 (variation numbers 1 to 5 equal to 0, 1, 2, 3, and 4 wt.% Cu addition, consecutively), indicate that the highest hardness of 113.4 BHN was observed in the specimen with 4 wt.% Cu, specifically in the outer region (Segment 1). Conversely, the lowest hardness of 75.4 BHN was recorded in the specimen with 1 wt.% Cu, in Segment 3. These findings suggest that adding Cu increases the specimen's hardness. The increase in hardness is directly proportional to the rise in porosity, meaning that as Cu content increases, both hardness and porosity tend to rise. Additionally, the increase in hardness is influenced by grain size, whereby the outer region exhibits finer and smaller grains. This finding is in accordance with existing research, which indicates that the hardness of the casting results from the centrifugal method will increase the hardness of the outer surface. The increase in hardness is influenced by the centrifugal force that pushes the copper powder to the outer side, as the density of copper is greater. Consequently, the addition of 4 wt.% copper will increase the hardness on the outer side. The results of other studies indicate that casting hardness increases with increasing porosity. The increase in hardness is also related to grain distribution: grains are finer (smaller) on the outer surface, which increases the grain-boundary area per unit volume of the metal, thereby increasing the metal's strength.

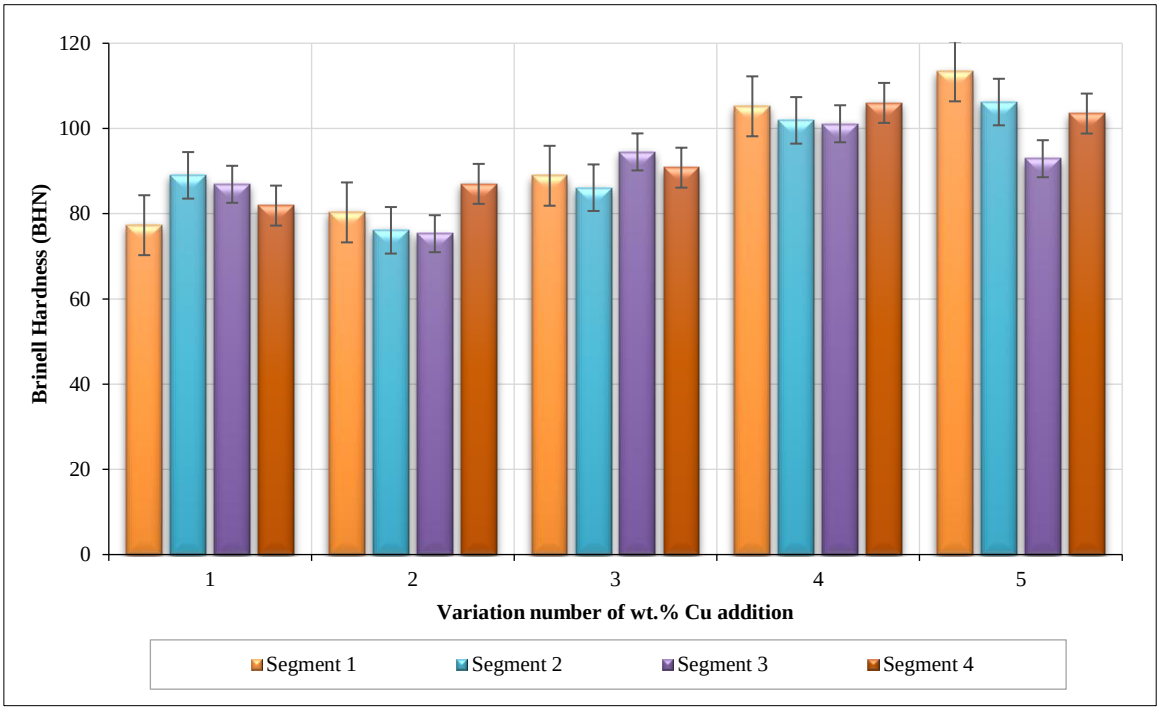


**Figure 8. Hardness test results for Cu addition**

The above process results in a larger surface area subjected to hardness testing, consequently leading to higher hardness values at the outer region. Furthermore, the presence of the $Al_2Cu$ phase at the outer diameter, particularly in Segments 3 and 4, contributes to the increased hardness due to the centrifugal force effect. The data presented in Figure 9 illustrates the impact of $SiO_2$ particle addition on hardness, measured from Segment 1 (outer region) to Segment 4 (inner region) along the specimen's cross-section (variation numbers 1 to 4 equal to 0, 3, 6, and 9 wt.% $SiO_2$ addition, consecutively). Each segment was divided into three hardness testing points, and the average value for each segment was recorded. The hardness values for the percentage of 0 wt.% $SiO_2$ particles are 77 HRB (outer part), 89 HRB, 87 HRB, and 82 HRB (inner part). The rate of 3 wt.% $SiO_2$ particles is 83 HRB (outer part), 95 HRB, 98 HRB, and 92 HRB (inner part). The values of 6 wt.% $SiO_2$ particles are 78 HRB (outer part), 81 HRB, 81 HRB, and 76 HRB (inner part). The rate of 9 wt.% $SiO_2$ particles is 76 HRB (outer part), 88 HRB, 78 HRB, and 81 HRB (inner part). The hardness values increased with the addition of $SiO_2$ particles, particularly from 0 wt.% to 3 wt.% $SiO_2$. However, a decrease in hardness was observed at 6 wt.% and 9 wt.% $SiO_2$. The hard surface of $SiO_2$ particles enhances the toughness and

hardness of the composite material [70-76]. The decrease in hardness for specimens with 6 wt.% and 9 wt.% $SiO_2$ compared to those with 3 wt.% $SiO_2$ is attributed to the fact that the hardness of aluminum-based composites with $SiO_2$ reinforcement reaches an optimal level and subsequently declines as the $SiO_2$ content exceeds 5% [64].

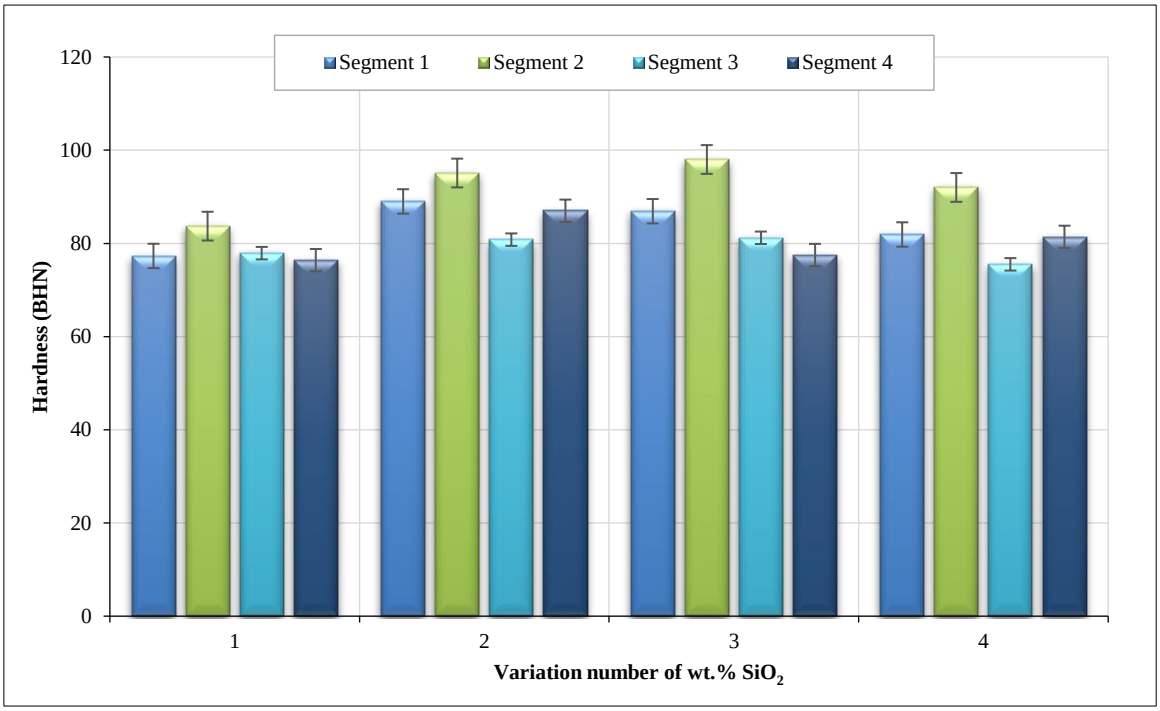


**Figure 9. Hardness test results due to $SiO_2$ addition**

The hardness data obtained after the addition of $SiO_2$ particles indicate that the inner region of the specimen tends to exhibit higher hardness values than the outer region. In centrifugal casting, particles with lower density tend to accumulate in the inner layer, while those with higher density migrate toward the outer layer. Because the density of $SiO_2$ (2.65 g/cm³) [5] is slightly lower than that of the Al–Si matrix, the $SiO_2$ particles are less strongly driven outward by the centrifugal force and therefore become more concentrated toward the central or inner region of the casting. This non-uniform particle distribution results in a functionally graded microstructure, where the inner segment has a higher volume fraction of hard ceramic particles compared to the outer segment. From the standpoint of material hardness theories for particle-reinforced metal matrix composites, this higher local $SiO_2$ content naturally promotes an increase in hardness. $SiO_2$ is a stiff, brittle ceramic phase with much higher intrinsic hardness than the surrounding Al–Si matrix; its presence therefore provides dispersion strengthening. Under indentation or local loading, part of the applied stress is transferred from the softer aluminum matrix to the harder $SiO_2$ particles (load-transfer mechanism), thereby increasing the resistance to plastic deformation.

In addition, the rigid particles act as obstacles to dislocation motion: dislocations are pinned at the particle–matrix interfaces or forced to bypass the particles via mechanisms analogous to Orowan looping. This restriction of dislocation mobility elevates the critical stress required for further plastic flow, which manifests macroscopically as higher hardness values. If $SiO_2$ particles also act as heterogeneous nucleation sites during solidification, they may refine the microstructure locally; based on grain refinement and Hall–Petch-type theories, smaller effective grain or cell sizes further increase hardness by increasing the grain boundary area that impedes dislocation motion. Consequently, even though the inner region may exhibit slightly higher porosity than the outer region—which on its own would tend to reduce hardness—the strengthening effect induced by the higher $SiO_2$ particle content can dominate, resulting in a net increase in hardness in the inner segment. Thus, the observed hardness gradient, with higher hardness toward the inner region, is consistent with the combined effects of centrifugal particle segregation and classical strengthening theories for ceramic-particle-reinforced aluminum alloys.

The specimen exhibited a decrease in hardness after the addition of $SiO_2$ particles at concentrations of 6 wt.% and 9 wt.%. One factor contributing to this reduction is the variation in porosity levels across different specimen regions. Porosity is inversely proportional to density, meaning that higher density results in lower porosity [64]. Pores in the composite may form due to gaps between reinforcement particles not filled by molten aluminum, making porosity one of the primary factors affecting the composite's mechanical properties [64]. The hardness of the specimen with a 9 wt.%

$SiO_2$ particle concentration in Segment 3 decreased, as observed in the microstructure. This region exhibits a limited presence of the Al-Si phase. It predominantly comprises the α-Aluminum phase, with only a miniscule amount of $SiO_2$ particles distributed within the segment.

## 5. Microstructural Observation and Analysis

### 5.1. Effect of Copper (Cu) Addition

The microstructural observations of Cu addition are presented in Figures 10 and 11. The phases formed in the Al-Si alloy produced by means of centrifugal casting with Cu addition include primary α-Aluminum, the Al-Si eutectic phase, and the $Al_2$ Cu intermetallic phase, which are typical constituents of Al–Si–Cu cast alloys, as predicted by the Al–Si–Cu phase diagram.

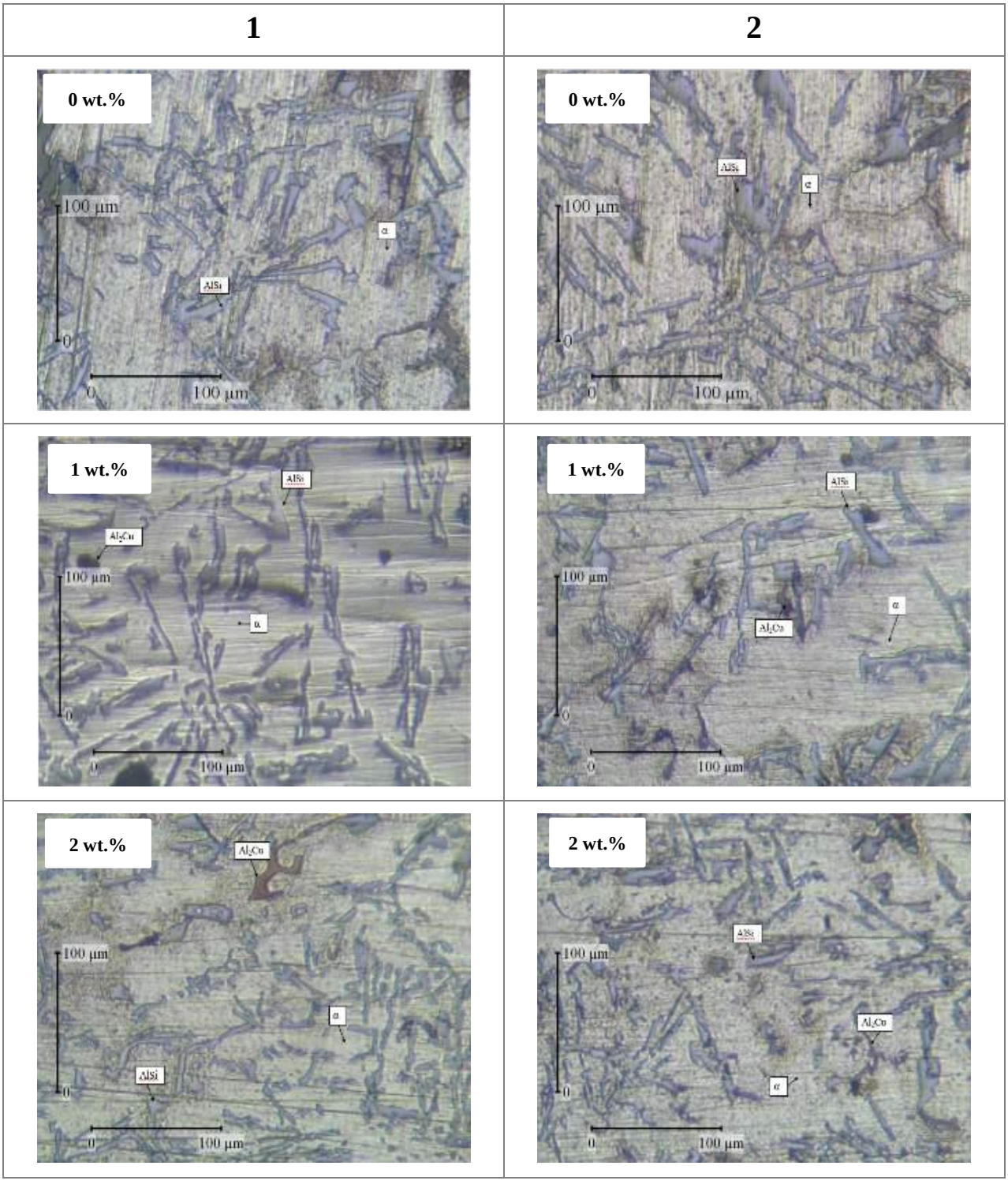


**(a)**

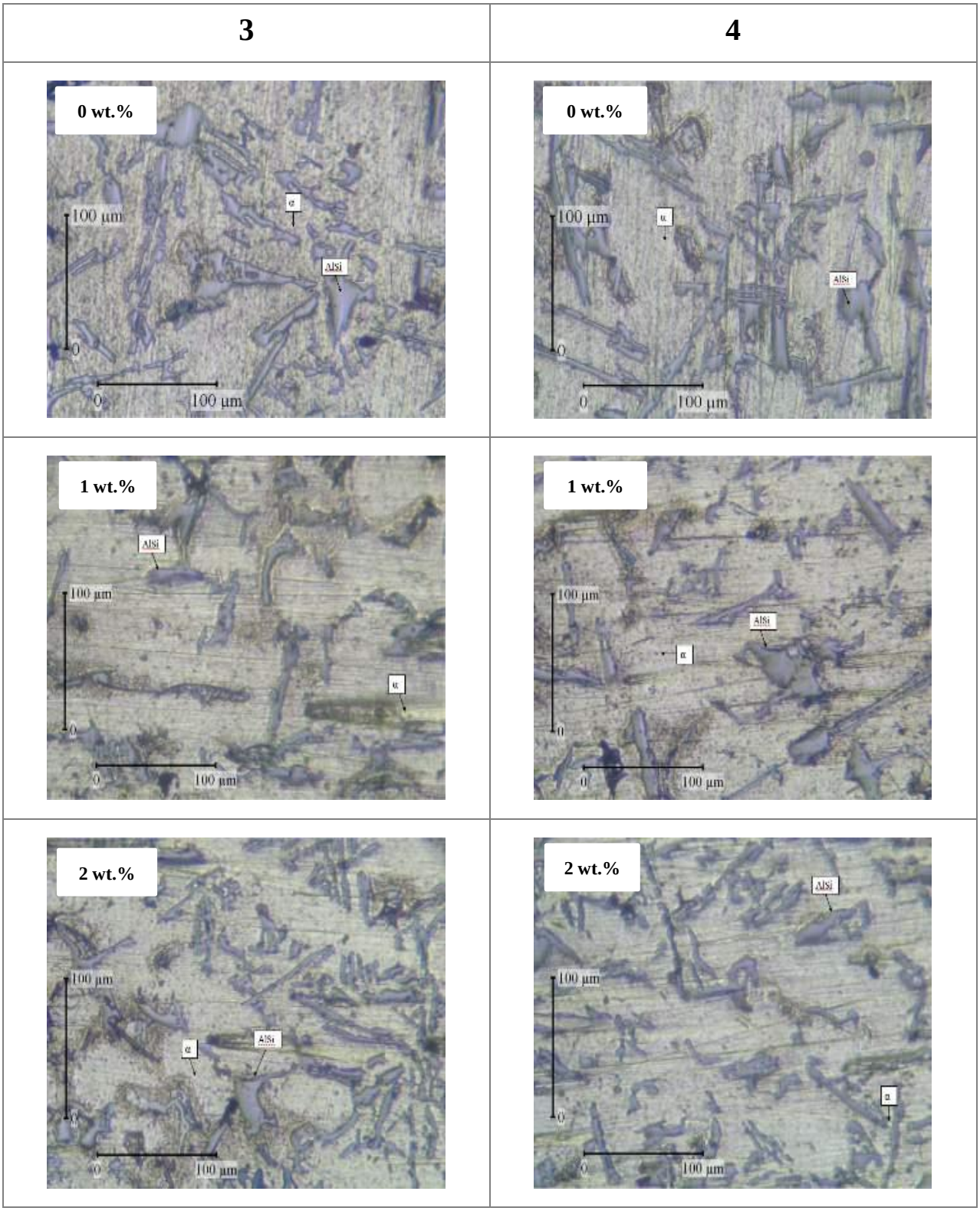


**(b)**

**Figure 10. Microstructural images of each segment following Cu additions of 0-2 wt.%: (a) Segments 1 and 2 and (b) Segments 3 and 4**

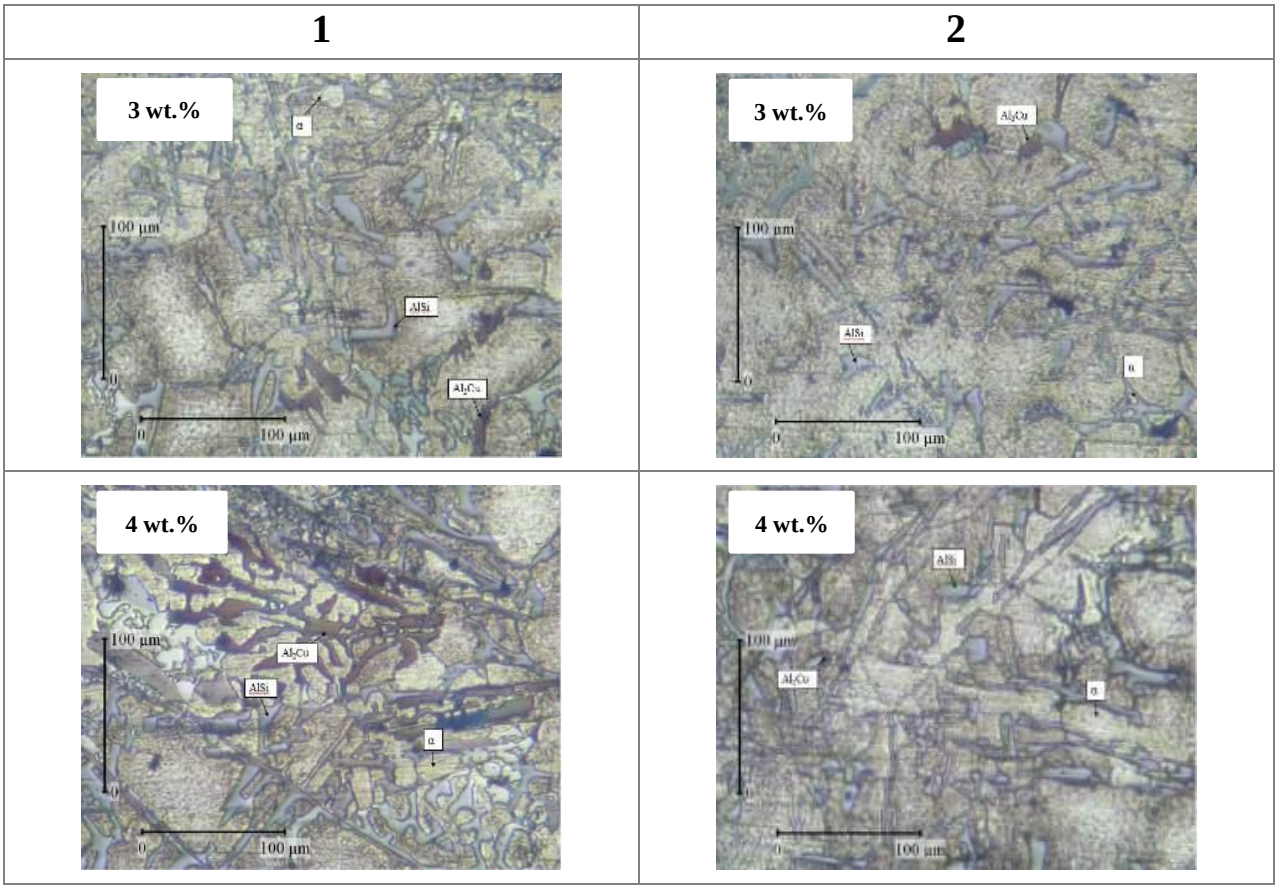


**(a)**

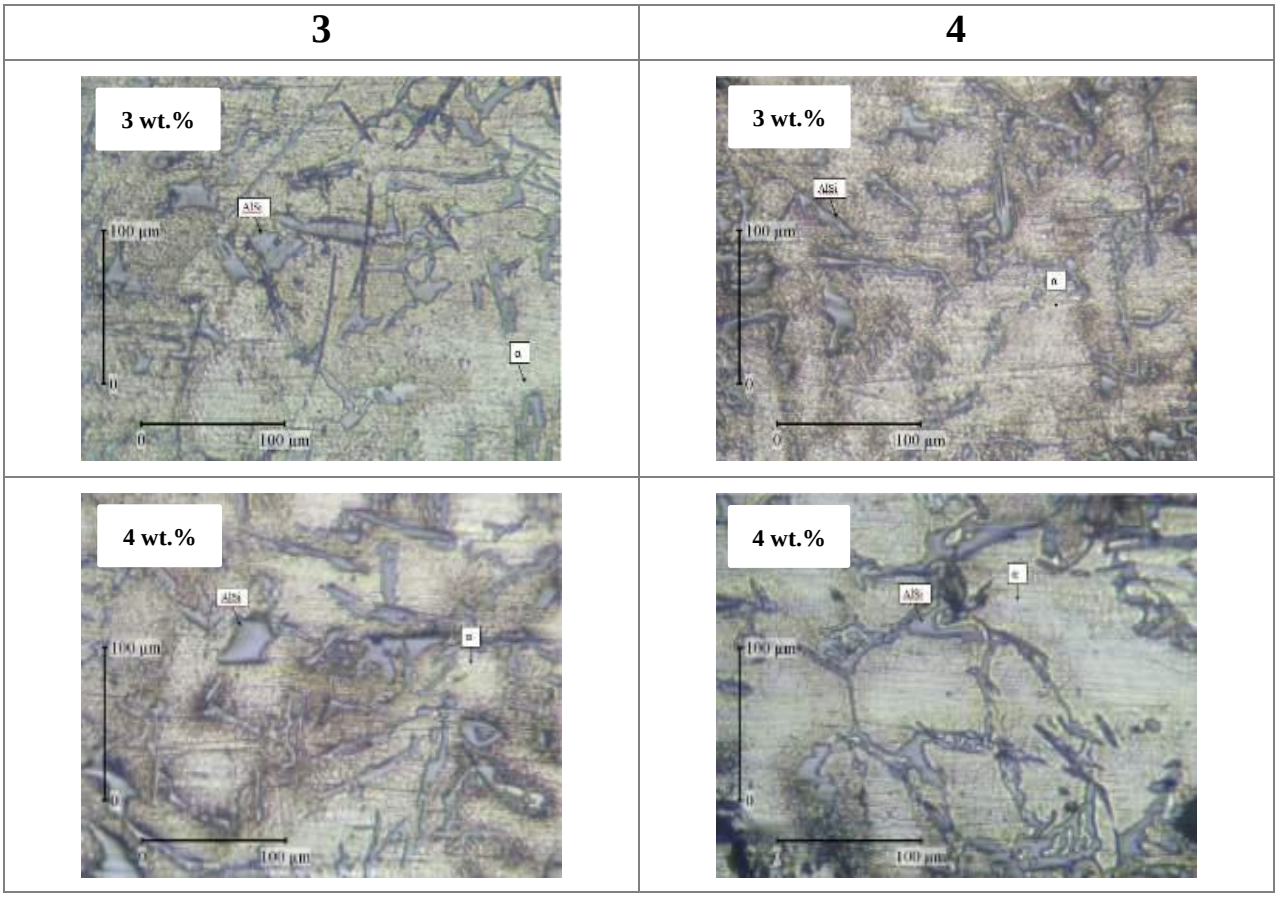


**(b)**

**Figure 11. Microstructural images of each segment following Cu additions of 3-4 wt.%: (A) Segments 1 and 2 and (B) Segments 3 and 4**

In the present study, the Al-Si eutectic phase is more prominently visible in the microstructure, whereas the $Al_2$ Cu phase is more frequently observed in Segments 3 and 4 of the outer regions of the specimen. This distribution can be explained by centrifugal segregation and density differences: Cu has a higher density than both Al and Si; therefore, during rotation, it experiences a larger centrifugal force and migrates preferentially toward the outer diameter, where it enriches the interdendritic regions and promotes the local formation of $Al_2Cu$. This finding is consistent with the theory of centrifugal casting, in which heavier solute-rich liquid and intermetallic phases are driven outward, while lighter phases remain closer to the inner region. The microstructure also reveals that the grain size tends to be smaller and more elongated in the outer diameter region. In contrast, the grains in the inner diameter region are coarser and more equiaxed. This gradient can be correlated with solidification theory and heat transfer considerations.

When the molten metal is forced against the mold wall by centrifugal force, the outer region experiences a higher adequate pressure and a much higher cooling rate due to direct contact with the relatively cold mold. Based on classical solidification theory, an increased cooling rate reduces the time available for grain growth, leading to finer grains and a smaller secondary dendrite arm spacing in the outer layer. This rapid extraction of heat also causes initial "skin solidification," whereby a thin solidified layer forms almost immediately after pouring, effectively freezing the outer microstructure and limiting subsequent coarsening. Toward the inner region, the cooling rate decreases because heat must be conducted through the already solidified shell. Hence, grains and eutectic colonies have more time to grow and coarsen, resulting in a larger, more pronounced microstructure consistent with grain growth kinetics.

From a mechanical metallurgy perspective, this microstructural refinement in the outer region is closely related to strength and hardness theories such as the Hall–Petch relationship, which states that smaller grain size increases resistance to dislocation motion and thus enhances hardness and yield strength. In addition, the presence of finely dispersed $Al_2Cu$ in the outer segments contributes to precipitation and dispersion strengthening, as hard intermetallic particles impede dislocation movement and locally increase the hardness of the matrix. However, the microstructure also shows porosity, visible as dark regions in the images. This porosity is associated with both gas and shrinkage mechanisms and becomes more pronounced with increasing Cu content, as reflected in the porosity measurements. Higher Cu levels modify solidification behavior, reduce feeding efficiency in interdendritic regions, and promote the formation of shrinkage cavities and gas pores trapped between growing dendrites. The observed porosity distribution is consistent with the porosity calculations. It supports the earlier finding that increased Cu content leads to a higher porosity level [8], which, in turn, can locally reduce the effective load-bearing area and partially offset the strengthening benefits of grain refinement and $Al_2Cu$ formation.

### 5.2. Effect of Silica ($SiO_2$) Addition

Microstructural analysis of the specimen (Figures 12 and 13) reveals the presence of α-Aluminum and Al-Si eutectic phases in all compositions, whereas $SiO_2$ particles are clearly observed in specimens containing 3 wt.%, 6 wt.%, and 9 wt.% $SiO_2$. Apart from the 0 wt.% $SiO_2$ composition, these $SiO_2$ particles are predominantly located in Segments 3 and 4, with a higher concentration in Segment 4. This distribution is consistent with centrifugal casting theory for systems in which the reinforcement has a lower density than the metallic matrix: because the density of $SiO_2$ is slightly lower than that of the Al–Si melt, the effective centrifugal force acting on the particles is smaller than that on the liquid metal; therefore, the matrix is driven more strongly toward the mold wall. Concurrently, the lighter $SiO_2$ tends to remain closer to the inner region. High rotational speeds generate a distinct radial segregation profile, with a region enriched in fine particles toward the inner side of the wall thickness [77]. From Figures 12 and 13, it is also evident that there is a clear difference in grain morphology between segments. First, in terms of grain size, all $SiO_2$-containing specimens exhibit a trend whereby the grain size gradually increases from Segment 1 (outermost) to Segment 4 (innermost).

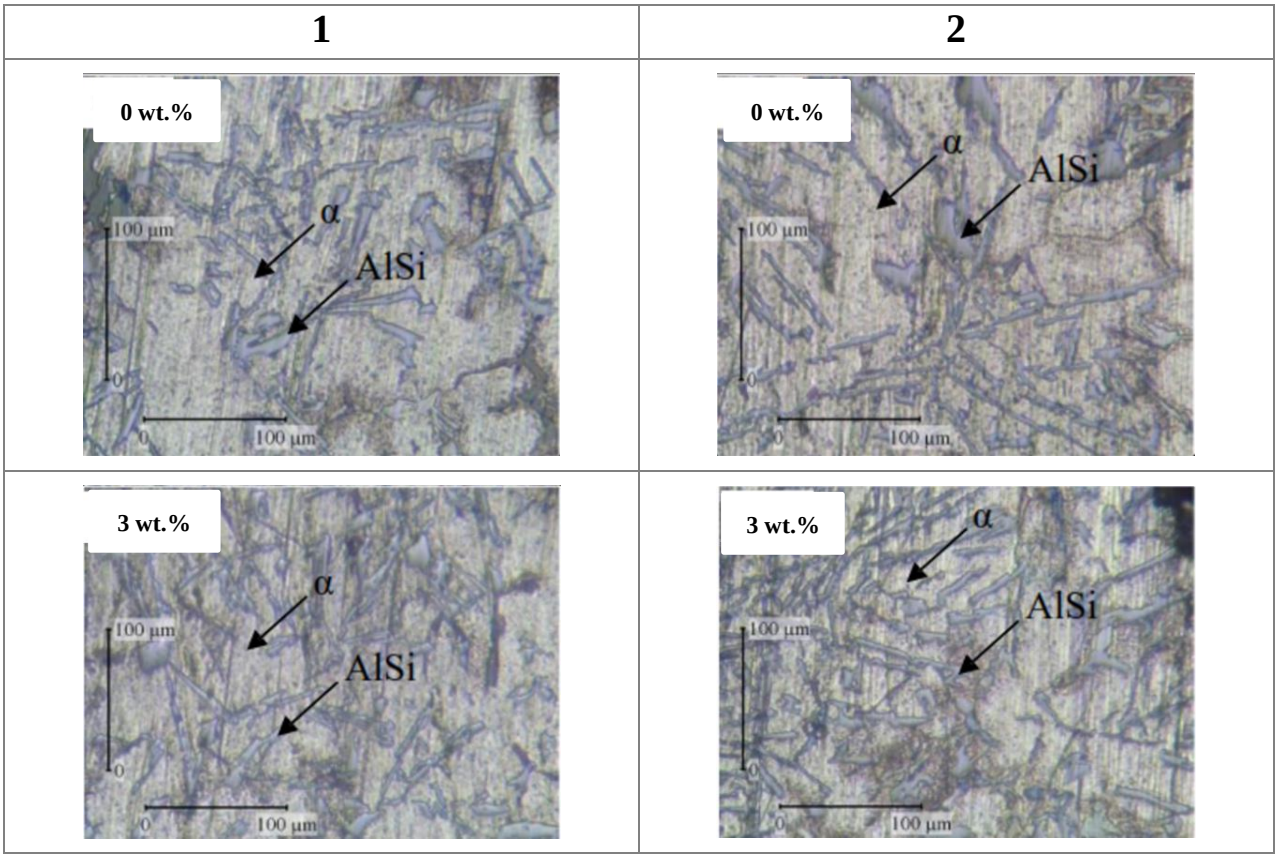


**(a)**

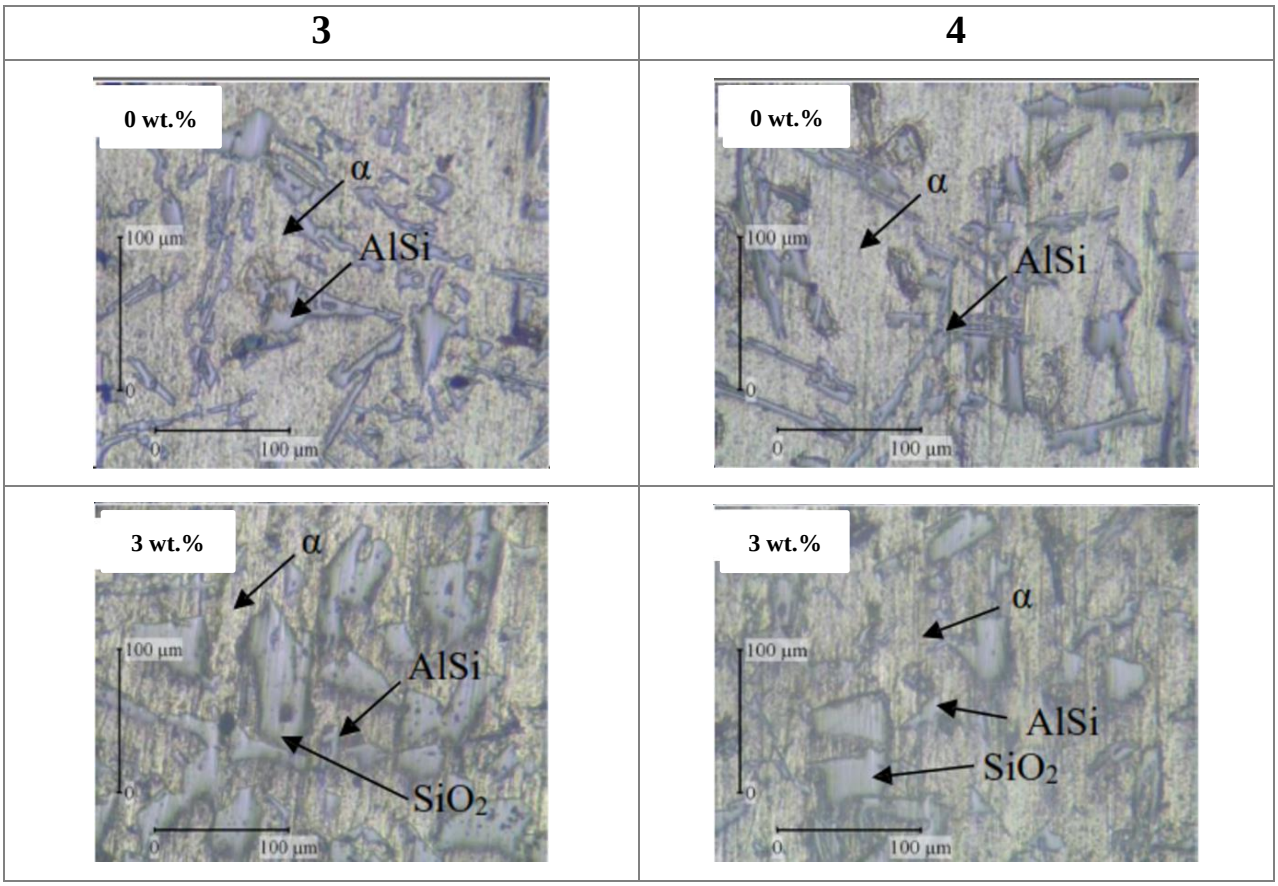


**(b)**

**Figure 12. Microstructural images of each segment following $SiO_2$ additions of 0-3 wt.%: (a) Segments 1 and 2 and (b) Segments 3 and 4**

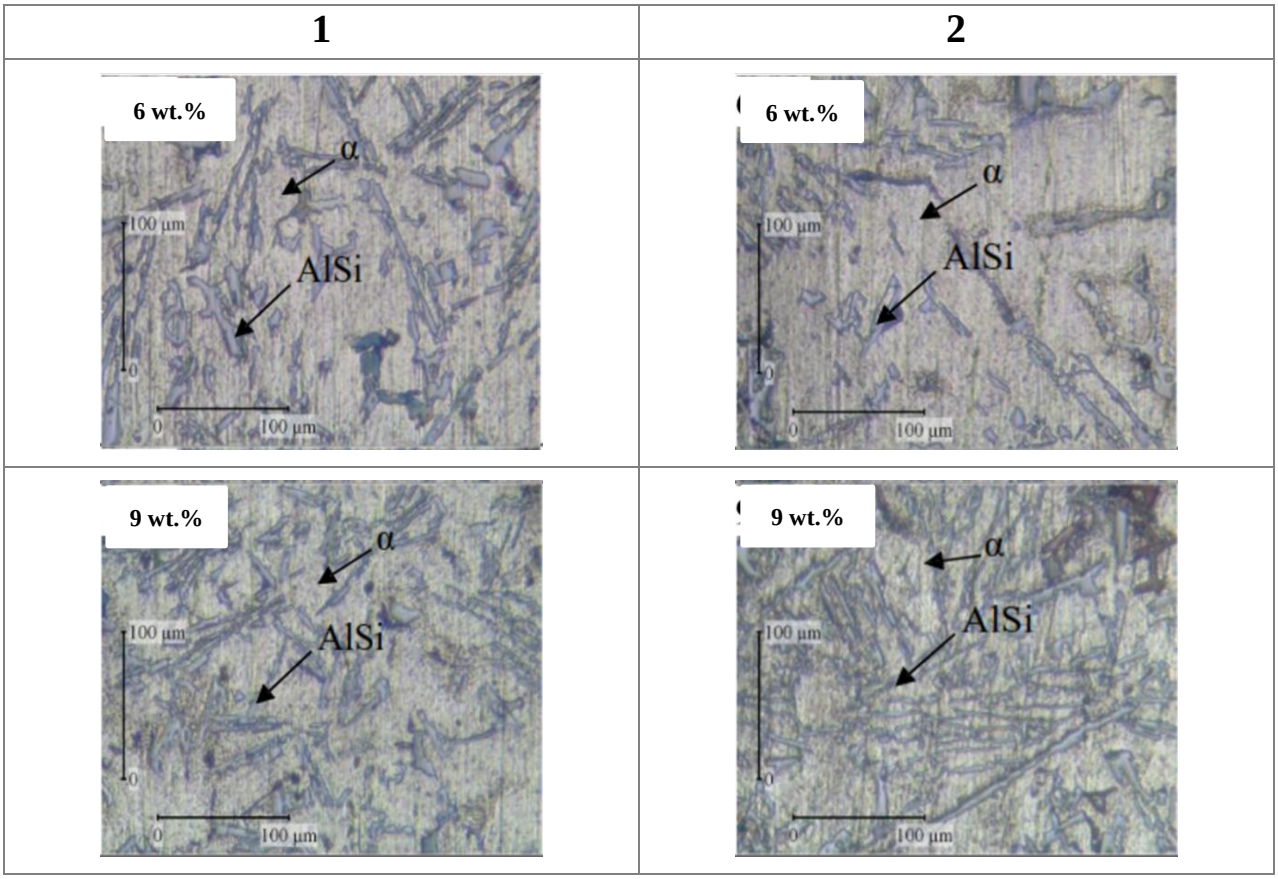


**(a)**

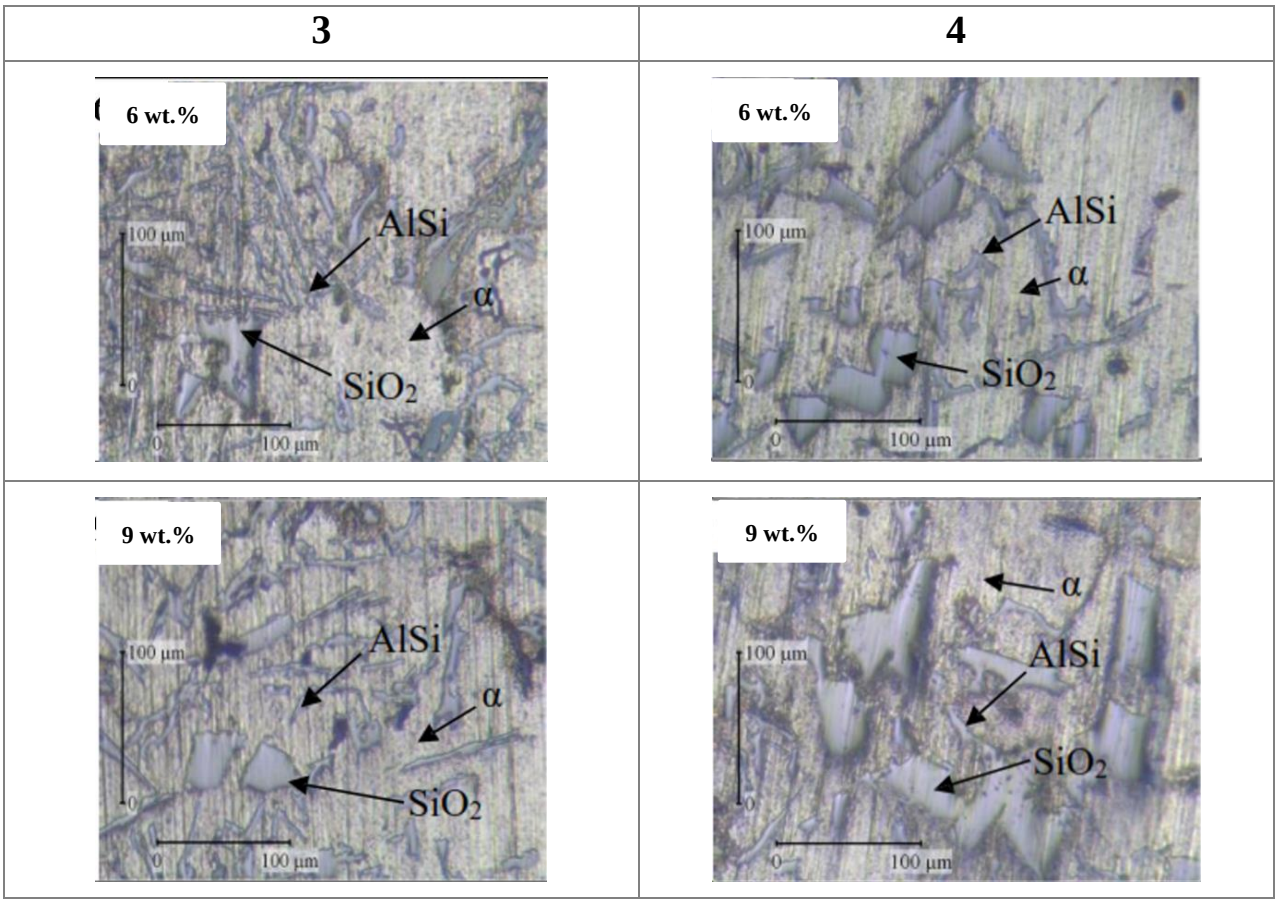


**(b)**

**Figure 13. Microstructural images of each segment following $SiO_2$ additions of 6-9 wt.%: (a) Segments 1 and 2 and (b) Segments 3 and 4**

This gradient can be directly linked to classical grain growth and solidification theories: the outermost region, in direct contact with the mold wall, experiences the highest cooling rate and most significant temperature gradient, which promotes a high nucleation rate but limits the time available for grain growth, resulting in finer, more refined grains. As solidification progresses inward, the local cooling rate decreases, providing grains and eutectic colonies more time to coarsen; thus, the deeper (inner) regions inevitably develop larger grain sizes.

Regarding the composition of the phase/structure formed, the added $SiO_2$ tends to be distributed in the inner region (Segments 3 and 4) because of its lower density relative to the Al–Si matrix. Centrifugal force will preferentially push elements or phases with higher density outward, creating an element/phase segregation pattern in which the metallic matrix becomes richer near the outer surface and the lighter ceramic particles become enriched toward the inner region. From the standpoint of grain theory, this segregation not only alters local composition but can also influence nucleation behavior. $SiO_2$ particles may act as heterogeneous nucleation sites (particle-stimulated nucleation), locally increasing the number of nuclei; however, because the cooling rate is lower in the inner region, these nuclei have more time to grow, leading to a microstructure that contains both particle clusters and coarser grains. Results presented in the literature on centrifugal casting of metal matrix composites show that, for systems where the reinforcement is denser than the matrix, particles tend to accumulate near the outer surface. Concurrently, the central section of the tube wall exhibits a eutectic microstructure with primary aluminum [57]. In contrast, in the present system with lower-density $SiO_2$ reinforcement, the centrifugal force is not sufficient to drive the particles fully toward the outermost layer; instead, they remain concentrated in the inner segments [77]. In terms of mechanical metallurgy, the finer grains in the outer region are expected—based on the Hall–Petch relationship—to provide higher strength and hardness. In contrast, the coarser grains in the inner region may reduce strength but are accompanied by a higher volume fraction of hard $SiO_2$ particles, resulting in a complex balance between grain-size softening and particle strengthening. Thus, the observed microstructural gradient—finer grains and matrix-rich outer region, coarser grains and $SiO_2$-rich inner region—is entirely consistent with grain growth kinetics, heterogeneous nucleation concepts, and centrifugal segregation theories for functionally graded metal matrix composites.

## 6. Conclusions

- The porosity of cast specimens tends to increase with the addition of copper. In contrast, the porosity of each segment decreases from the inner diameter (Segment 4) to the outer diameter (Segment 1). In contrast, specimens with added $SiO_2$ exhibit a reduction in density as the $SiO_2$ particle concentration increases.
- The microstructure of the cast specimens reveals that the grain distribution on the outer surface is denser, with smaller, elongated grains. In contrast, the inner region exhibits a more dispersed grain distribution with larger grain sizes.
- Microstructural analysis results show that the distribution of $SiO_2$ particles is primarily concentrated in Segments 3 and 4, which are located near the specimen's center.
- The addition of copper to Al-Si alloys using centrifugal casting enhances hardness, particularly on the outer surface of the specimen. Conversely, adding $SiO_2$ particles in vertical-axis centrifugal casting increases the hardness, primarily in the inner regions near the rotational axis.

## 7. Declarations

### 7.1. Author Contributions

Conceptualization, T.T. and E.S.; methodology, T.T. and Tr.Tr.; software, A.R.P.; validation, T.T., E.S., and Tr.Tr.; formal analysis, T.T.; investigation, T.T.; resources, E.S. and Tr.Tr.; data curation, A.R.P.; writing—original draft preparation, T.T.; writing—review and editing, A.R.P., B.D., and H.C.; visualization, P.W.A. and M.I.S.; supervision, E.S., A.R.P., and Tr.Tr.; project administration, A.R.P.; funding acquisition, A.R.P. All authors have read and agreed to the published version of the manuscript.

### 7.2. Data Availability Statement

The data presented in this study are available on request from the corresponding author.

### 7.3. Funding

This work was supported by the RKAT Universitas Sebelas Maret—Year 2025, under the Research Scheme of "PENGUATAN KAPASITAS GRUP RISET" (PKGR-UNS) A, with research grant/contract no. 371/UN27.22/PT.01.03/2025. The authors highly acknowledge this support.

### 7.4. Conflicts of Interest

The authors declare no conflict of interest.

## 8. References

[1] Jia, L., Xu, D., Li, M., Guo, J., & Fu, H. (2012). Casting defects of Ti-6Al-4V alloy in vertical centrifugal casting processes with graphite molds. Metals and Materials International, 18(1), 55-61. doi:10.1007/s12540-012-0007-0.

[2] Ping, W. S., Rong, L. D., Jie, G. J., Yun, L. C., Qing, S. Y., & Zhi, F. H. (2006). Numerical simulation of microstructure evolution of Ti-6Al-4V alloy in vertical centrifugal casting. Materials Science and Engineering: A, 426(1–2), 240–249. doi:10.1016/j.msea.2006.04.014.

[3] Chirita, G., Soares, D., & Silva, F. S. (2008). Advantages of the centrifugal casting technique for the production of structural components with Al-Si alloys. Materials and Design, 29(1), 20–27. doi:10.1016/j.matdes.2006.12.011.

[4] Ali, S. M. (2019). The effect of reinforced SiC on the mechanical properties of the fabricated hypoeutectic Al-Si alloy by centrifugal casting. Engineering Science and Technology, an International Journal, 22(4), 1125–1135. doi:10.1016/j.jestch.2019.02.009.

[5] Madhusudhan, Narendranath, S., Kumar, G. C. M., & Mukunda, P. G. (2010). Experimental study on rate of solidification of centrifugal casting. International Journal of Mechanical and Materials Engineering, 5(1), 101–105.

[6] Shailesh, P., Praveen Kumar, B., Sundarrajan, S., & Komariahia, M. (2012). Experimental investigation on centrifugal casting of 5500 alloy: A Taguchi approach. Scientific Research and Essays, 7(44), 3797–3808.

[7] Jamian, S., Ayob, S. N., Abidin, M. R. Z., & Muhd Nor, N. H. (2016). Fabrication of functionally graded natural fibre/epoxy cylinder using centrifugal casting method. ARPN Journal of Engineering and Applied Sciences, 11(4), 2327–2331.

[8] Prasad, K. S. K., Murali, M. S., & Mukunda, P. G. (2010). Analysis of fluid flow in centrifugal casting. Signal, Image and Video Processing, 4(1), 103–110. doi:10.1007/s11706-010-0005-4.

[9] Naebe, M., & Shirvanimoghaddam, K. (2016). Functionally graded materials: A review of fabrication and properties. Applied Materials Today, 5, 223–245. doi:10.1016/j.apmt.2016.10.001.

[10] Li, Y., Feng, Z., Hao, L., Huang, L., Xin, C., Wang, Y., Bilotti, E., Essa, K., Zhang, H., Li, Z., Yan, F., & Peijs, T. (2020). A Review on Functionally Graded Materials and Structures via Additive Manufacturing: From Multi-Scale Design to Versatile Functional Properties. Advanced Materials Technologies, 5(6), 1900981. doi:10.1002/admt.201900981.

[11] Ma, Z., Liu, W., Li, W., Liu, H., Song, J., Liu, Y., Huang, Y., Xia, Y., Wang, Z., Liu, B., Lv, Z., Hu, G., Wang, T., Li, T., Liu, S., & Zhang, Y. (2024). Additive manufacturing of functional gradient materials: A review of research progress and challenges. Journal of Alloys and Compounds, 971, 170768. doi:10.1016/j.jallcom.2023.172642.

[12] Shan, Z., Tran, M. T., Woo, W., Hwang, S. K., Wang, H., Luzin, V., Kingston, E. J., Hill, M. R., DeWald, A., & Kim, D. K. (2023). Multiscale framework for prediction of residual stress in additively manufactured functionally graded material. Additive Manufacturing, 61, 103378. doi:10.1016/j.addma.2022.103378.

[13] Pradeep, A. D., & Rameshkumar, T. (2021). Review on centrifugal casting of functionally graded materials. Materials Today: Proceedings, 45, 729–734. doi:10.1016/j.matpr.2020.02.764.

[14] Watanabe, Y., Inaguma, Y., Sato, H., & Miura-Fujiwara, E. (2009). A novel fabrication method for functionally graded materials under centrifugal force: The centrifugal mixed-powder method. Materials, 2(4), 2510–2525. doi:10.3390/ma2042510.

[15] Kumar, N., & Panigrahi, S. K. (2025). A casting strategy to develop high-performance Al-Si cast alloy. Manufacturing Letters, 44, 1731-1738. doi:10.1016/j.mfglet.2025.06.192.

[16] Radhika, N., & Raghu, R. (2016). Development of functionally graded aluminium composites using centrifugal casting and influence of reinforcements on mechanical and wear properties. Transactions of Nonferrous Metals Society of China, 26(4), 905–916. doi:10.1016/S1003-6326(16)64185-7.

[17] El-Galy, I. M., Ahmed, M. H., & Bassiouny, B. I. (2017). Characterization of functionally graded Al-SiCp metal matrix composites manufactured by centrifugal casting. Alexandria Engineering Journal, 56(4), 371–381. doi:10.1016/j.aej.2017.03.009.

[18] Verma, R. K., Parganiha, D., & Chopkar, M. (2021). A review on fabrication and characteristics of functionally graded aluminum matrix composites fabricated by centrifugal casting method. SN Applied Sciences, 3(2), 227. doi:10.1007/s42452-021-04200-8.

[19] Milosan, I., Bedő, T., Gabor, C., Munteanu, D., Pop, M. A., Catana, D., Cosnita, M., & Varga, B. (2021). Characterization of Aluminum Alloy–Silicon Carbide Functionally Graded Materials Developed by Centrifugal Casting Process. Applied Sciences, 11(4), 1625. doi:10.3390/app11041625.

[20] Mohapatra, S., Sarangi, H., & Mohanty, U. K. (2020). Effect of processing factors on the characteristics of centrifugal casting. Manufacturing Review, 7, 26. doi:10.1051/mfreview/2020024.

[21] Mazloum, K., Al Njjar, A., & Sata, A. (2024). Exploring the Filling Related Defect in Vertical Centrifugal Castings for A413 and A356 Using 3D Transient Simulation. Recent Patents on Mechanical Engineering, 18(4), 410–419. doi:10.2174/0122127976320259240626094431.

[22] Shen, X., Yin, Y., Xiao, G., Ji, X., & Zhou, J. (2019). Physical simulation of fluid frontal motion morphology in filling process of titanium alloy vertical centrifugal casting. Procedia Manufacturing, 37, 51–58. doi:10.1016/j.promfg.2019.12.011.

[23] Ling, Y., Zhou, J., Nan, H., Zhu, L., & Yin, Y. (2018). A shrinkage cavity model based on pressure distribution for Ti-6Al–4V vertical centrifugal castings. Journal of Materials Processing Technology, 251, 295–304. doi:10.1016/j.jmatprotec.2017.08.025.

[24] Liao, M., Zhang, C., Liu, G., & Wang, Z. (2025). Microstructural evolution and superplasticity of IN718 superalloy rings via vacuum centrifugal casting, thermo-mechanical controlled ring rolling and standard heat treatment. Materials Science and Engineering: A, 947, 149275. doi:10.1016/j.msea.2025.149275.

[25] Changyun, L., Haiyan, W., Shiping, W., Lei, X., Kuangfei, W., & Hengzhi, F. (2010). Research on Mould Filling and Solidification of Titanium Alloy in Vertical Centrifugal Casting. Rare Metal Materials and Engineering, 39(3), 388–392. doi:10.1016/s1875-5372(10)60085-9.

[26] Changyun, L., Shiping, W., Jingjie, G., Yanqing, S., Weisheng, B., & Hengzhi, F. (2006). Model experiment of mold filling process in vertical centrifugal casting. Journal of Materials Processing Technology, 176(1–3), 268–272. doi:10.1016/j.jmatprotec.2006.04.004.

[27] ASTM E10-18. (2023). ASTM E10 Standard Test Method for Brinell Hardness of Metallic Materials -- eLearning Courses-ES. ASTM Standard, Pennsylvania, United States. doi:10.1520/E0010-18.

[28] ASTM E407-07(2015)e1. (2023). Standard Practice for Microetching Metals and Alloys. ASTM Standard, Pennsylvania, United States. doi:10.1520/E0407-07R15E01.

[29] Davis, J. R. (Ed.). (1999). Corrosion of Aluminum and Aluminum Alloys. ASTM International, Pennsylvania, United States. doi:10.31399/asm.tb.caaa.9781627082990.

[30] Mondolfo, L. F. (2013). Aluminum alloys: structure and properties. Elsevier, Amsterdam, Netherlands.

[31] Deschamps, A., & Bréchet, Y. (1998). Influence of quench and heating rates on the ageing response of an Al-Zn-Mg-(Zr) alloy. Materials Science and Engineering: A, 251(1–2), 200–207. doi:10.1016/s0921-5093(98)00615-7.

[32] Marioara, C. D., Andersen, S. J., Jansen, J., & Zandbergen, H. W. (2003). The influence of temperature and storage time at RT on nucleation of the β″ phase in a 6082 Al-Mg-Si alloy. Acta Materialia, 51(3), 789-796. doi:10.1016/S1359-6454(02)00470-6.

[33] Ringer, S. P., & Hono, K. (2000). Microstructural evolution and age hardening in aluminium alloys: atom probe field-ion microscopy and transmission electron microscopy studies. Materials Characterization, 44(1–2), 101–131. doi:10.1016/S1044-5803(99)00051-0.

[34] Birbilis, N., Cavanaugh, M. K., & Buchheit, R. G. (2006). Electrochemical behavior and localized corrosion associated with Al7Cu2Fe particles in aluminum alloy 7075-T651. Corrosion Science, 48(12), 4202–4215. doi:10.1016/j.corsci.2006.02.007.

[35] Kok, M. (2005). Production and mechanical properties of Al2O3 particle-reinforced 2024 aluminium alloy composites. Journal of Materials Processing Technology, 161(3), 381–387. doi:10.1016/j.jmatprotec.2004.07.068.

[36] Ramesh, C. S., Keshavamurthy, R., Channabasappa, B. H., & Ahmed, A. (2009). Microstructure and mechanical properties of Ni-P coated Si3N4 reinforced Al6061 composites. Materials Science and Engineering: A, 502(1–2), 99–106. doi:10.1016/j.msea.2008.10.012.

[37] Chawla, N., & Shen, Y. L. (2001). Mechanical behavior of particle reinforced metal matrix composites. Advanced Engineering Materials, 3(6), 357–370. doi:10.1002/1527-2648(200106)3:6<357::AID-ADEM357>3.0.CO;2-I.

[38] Prasad, D. S., & Shoba, C. (2014). Hybrid composites - A better choice for high wear resistant materials. Journal of Materials Research and Technology, 3(2), 172–178. doi:10.1016/j.jmrt.2014.03.004.

[39] Natrayan, L., & Senthil Kumar, M. (2019). Mechanical, microstructure and wear behaviour of lm25/sic/mica metal matrix composite fabricated by squeeze casting technique. Applied Engineering Letters, 4(2), 72–77. doi:10.18485/aeletters.2019.4.2.5.

[40] Udupa, G., Rao, S. S., & Gangadharan, K. V. (2014). Functionally Graded Composite Materials: An Overview. Procedia Materials Science, 5, 1291–1299. doi:10.1016/j.mspro.2014.07.442.

[41] Mitrasinovic, A., Robles Hernández, F. C., Djurdjevic, M., & Sokolowski, J. H. (2006). On-line prediction of the melt hydrogen and casting porosity level in 319 aluminum alloy using thermal analysis. Materials Science and Engineering: A, 428(1–2), 41–46. doi:10.1016/j.msea.2006.04.084.

[42] Anyalebechi, P. N. (2013). Hydrogen-induced gas porosity formation in Al-4.5 wt% Cu-1.4 wt% Mg alloy. Journal of Materials Science, 48(15), 5342–5353. doi:10.1007/s10853-013-7329-2.

[43] Tiryakioğlu, M. (2020). The effect of hydrogen on pore formation in aluminum alloy castings: Myth versus reality. Metals, 10(3), 368. doi:10.3390/met10030368.

[44] Dash, M., & Makhlouf, M. (2001). Effect of key alloying elements on the feeding characteristics of aluminum-silicon casting alloys. Journal of Light Metals, 1(4), 251–265. doi:10.1016/S1471-5317(02)00002-0.

[45] Samuel, A. M., Samuel, E., Songmene, V., & Samuel, F. H. (2023). A Review on Porosity Formation in Aluminum-Based Alloys. Materials, 16(5). doi:10.3390/ma16052047.

[46] Yuan, W., Zhao, H. D., Shen, X., Zou, C., Liu, Y., & Xu, Q. Y. (2025). Numerical simulation of microstructure and microporosity morphology in directional solidification of aluminum-copper alloys: Effect of copper content and withdrawal rate. China Foundry, 22(1), 33–44. doi:10.1007/s41230-024-4014-9.

[47] Rajan, T. P. D., & Pai, B. C. (2011). Processing of functionally graded aluminium matrix composites by centrifugal casting technique. Materials Science Forum, 690, 157–161. doi:10.4028/www.scientific.net/MSF.690.157.

[48] Balout, B., & Litwin, J. (2012). Mathematical modeling of particle segregation during centrifugal casting of metal matrix composites. Journal of Materials Engineering and Performance, 21(4), 450–462. doi:10.1007/s11665-011-9873-8.

[49] Salifu, S., & Apata Olubambi, P. (2025). Influence of HEA reinforcement on pulse electric current sintered Aluminium Composites: Microstructure, Density, and nanomechanical properties. Materials Letters, 378, 137563. doi:10.1016/j.matlet.2024.137563.

[50] Xiao, L. Q., Shang, X. M., Zhao, Y., Li, J. W., Curran, H. J., & Chen, P. (2025). A comparative study of two methods for estimating aluminum agglomerate sizes: Cohen's pocket model and density-based clustering. Combustion and Flame, 273, 113957. doi:10.1016/j.combustflame.2024.113957.

[51] Yu, D. L., Jiang, B., Qi, X., Wang, C., & Song, R. G. (2024). Effect of current density on microstructure, mechanical behavior and corrosion resistance of black MAO coating on 6063 aluminum alloy. Materials Chemistry and Physics, 326, 129800. doi:10.1016/j.matchemphys.2024.129800.

[52] Li, Y., Wu, Z., Jing, Q., Zhang, L., Wang, D., Liu, Q., Qi, S., Xu, H., & Li, Y. (2024). Optimization effect and reaction mechanism of flake aluminum powder on the combustion performance of high-energy-density JP-10/PO composite fuel. Combustion and Flame, 262, 113369. doi:10.1016/j.combustflame.2024.113369.

[53] He, D., Chen, S. Bing, Lin, Y. C., Li, C., Xu, Z., & Xiao, G. (2023). Microstructural evolution characteristics and a unified dislocation-density related constitutive model for a 7046 aluminum alloy during hot tensile. Journal of Materials Research and Technology, 25, 2353–2367. doi:10.1016/j.jmrt.2023.06.008.

[54] Jung, J., Yoon, S., Gu, S., Kimura, Y., Toku, Y., & Ju, Y. (2023). Influence of a high-density pulsed electric current on the fatigue behaviour of prestrained aluminium alloys. Engineering Failure Analysis, 150, 107230. doi:10.1016/j.engfailanal.2023.107230.

[55] Zhang, G., Zhu, Z., Ning, J., & Feng, C. (2023). Dynamic impact constitutive relation of 6008-T6 aluminum alloy based on dislocation density and second-phase particle strengthening effects. Journal of Alloys and Compounds, 932, 167718. doi:10.1016/j.jallcom.2022.167718.

[56] Tjong, S. C., & Ma, Z. Y. (1997). The high-temperature creep behaviour of aluminium-matrix composites reinforced with SiC, Al2O3 and TiB2 particles. Composites Science and Technology, 57(6), 697–702. doi:10.1016/s0266-3538(97)00029-8.

[57] Zhang, S., & Wang, F. (2007). Comparison of friction and wear performances of brake materials containing different amounts of ZrSiO4 dry sliding against SiCp reinforced Al matrix composites. Materials Science and Engineering: A, 443(1–2), 242–247. doi:10.1016/j.msea.2006.09.054.

[58] Hu, M., Sun, D., & Zhu, M. (2024). Simulation of gas porosity formation and interaction with dendrite and eutectic structures during solidification of Al-Si alloys. Materials & Design, 241, 112977. doi:10.1016/j.matdes.2024.112977.

[59] Lu, W., Xing, H., Hu, R., Zhang, Q., & Yao, Z. (2023). The effect of wettability on gas porosity formation during directional solidification of alloys: Insights from lattice Boltzmann-cellular automata simulations. Journal of Materials Research and Technology, 22, 424–431. doi:10.1016/j.jmrt.2022.11.123.

[60] Zhang, A., Guo, Z., Jiang, B., Du, J., Wang, C., Huang, G., Zhang, D., Liu, F., Xiong, S., & Pan, F. (2021). Multiphase and multiphysics modeling of dendrite growth and gas porosity evolution during solidification. Acta Materialia, 214, 117005. doi:10.1016/j.actamat.2021.117005.

[61] Lu, W., Xing, H., Zhang, Q., Shen, Z., & An, Q. (2022). Modeling of microstructure formation with gas porosity growth during columnar dendritic solidification of aluminum alloys. Journal of Materials Research and Technology, 16, 1413–1421. doi:10.1016/j.jmrt.2021.12.078.

[62] Kang, H. J., Yoon, P. H., Lee, G. H., Park, J. Y., Jung, B. J., Lee, J. Y., Lee, C. U., Kim, E. S., & Choi, Y. S. (2021). Evaluation of the gas porosity and mechanical properties of vacuum assisted pore-free die-cast Al-Si-Cu alloy. Vacuum, 184, 109917. doi:10.1016/j.vacuum.2020.109917.

[63] Niklas, A., Orden, S., Bakedano, A., da Silva, M., Nogués, E., & Fernández-Calvo, A. I. (2016). Effect of solution heat treatment on gas porosity and mechanical properties in a die cast step test part manufactured with a new AlSi10MnMg(Fe) secondary alloy. Materials Science and Engineering: A, 667, 376–382. doi:10.1016/j.msea.2016.05.024.

[64] Debnath, S., Roy, S., & Pramanick, A. K. (2020). An Exploratory Comparative Study of Fabricated Silica-Aluminium Metal Matrix Composites with Casted Aluminium-Silicon Alloys. Journal of Physics: Conference Series, 1579(1), 12014. doi:10.1088/1742-6596/1579/1/012014.

[65] Zhu, M., Deng, C., Zhang, Z., Yang, D., Zhang, H., Wang, L., & Lu, X. (2025). Stereolithography 3D printing ceramics for ultrahigh strength aluminum matrix composites. Journal of Manufacturing Processes, 139, 126–132. doi:10.1016/j.jmapro.2025.02.037.

[66] Rajan, T. P. D., Pillai, R. M., & Pai, B. C. (2010). Characterization of centrifugal cast functionally graded aluminum-silicon carbide metal matrix composites. Materials Characterization, 61(10), 923–928. doi:10.1016/j.matchar.2010.06.002.

[67] Zhou, L., Chen, C., Yang, F., Han, W., & Guan, Q. (2020). Micropore structure characteristics and quantitative characterization methods of lacustrine shale-A case study from the member 2 of Kongdian Formation, Cangdong sag, Bohai Bay Basin. Petroleum Research, 5(2), 93–102. doi:10.1016/j.ptlrs.2020.01.001.

[68] Rabin, B. H., Smolik, G. R., & Korth, G. E. (1990). Characterization of entrapped gases in rapidly solidified powders. Materials Science and Engineering A, 124(1), 1–7. doi:10.1016/0921-5093(90)90328-Z.

[69] Du, Y., Chen, F., Cao, S., & Xie, R. J. (2024). Effect of an AC-DC composite longitudinal magnetic field on the microstructure and mechanical properties of WAAM Al-5 %Mg alloy. Materials Today Communications, 41, 110911. doi:10.1016/j.mtcomm.2024.110911.

[70] Šulak, I., Chlupova, A., Zalezak, T., Kubena, I., Roth, J. P., Jahns, K., Krupp, U., & Kruml, T. (2024). High-temperature Fatigue and Creep Performance of Additively Manufactured NiCu-based Alloy. Procedia Structural Integrity, 52, 143–153. doi:10.1016/j.prostr.2023.12.015.

[71] Sayuti, M., Sulaiman, S., Vijayaram, T. R., Baharudin, B. T. H., & Arifi, M. K. A. (2012). Manufacturing and Properties of Quartz ($SiO_2$) Particulate Reinforced Al-11.8%Si Matrix Composites. In Composites and Their Properties. IntechOpen Limited. doi:10.5772/48095.

[72] Raghvan, S., Singhal, P., Rattan, S., & Tyagi, A. K. (2023). Durable PP/EPDM/GF/$SiO_2$ nanocomposites with improved strength and toughness for orthotic applications. Journal of the Mechanical Behavior of Biomedical Materials, 138, 105582. doi:10.1016/j.jmbbm.2022.105582.

[73] Sant'Ana Gallo, L., Célarié, F., Bettini, J., Rodrigues, A. C. M., Rouxel, T., & Zanotto, E. D. (2022). Fracture toughness and hardness of transparent MgO–Al2O3–$SiO_2$ glass-ceramics. Ceramics International, 48(7), 9906–9917. doi:10.1016/j.ceramint.2021.12.195.

[74] Daguano, J. K. M. F., Suzuki, P. A., Strecker, K., Fernandes, M. H. F. V., & Santos, C. (2012). Evaluation of the micro-hardness and fracture toughness of amorphous and partially crystallized 3CaO·$P_2O_5$-$SiO_2$-MgO bioglasses. Materials Science and Engineering: A, 533, 26–32. doi:10.1016/j.msea.2011.10.117.

[75] Wei, W., Wang, Q., Chen, R., Zheng, C., & Su, Y. (2024). Improved toughness and oxidation resistance of Nb–Si based ultra-high temperature alloys by in-situ generated $La_2O_3$ phase. Materials Characterization, 208, 113686. doi:10.1016/j.matchar.2024.113686.

[76] Nishiyama, N., Seike, S., Hamaguchi, T., Irifune, T., Matsushita, M., Takahashi, M., Ohfuji, H., & Kono, Y. (2012). Synthesis of nanocrystalline bulk $SiO_2$ stishovite with very high toughness. Scripta Materialia, 67(12), 955–958. doi:10.1016/j.scriptamat.2012.08.028.

[77] Radhika, N., & Raghu, R. (2015). Experimental investigation on abrasive wear behavior of functionally graded aluminum composite. Journal of Tribology, 137(3), 31606. doi:10.1115/1.4029941.